AGU PUBLICATIONS

JGR

Journal of Geophysical Research: Planets

RESEARCH ARTICLE
10.1002/2015JE004951

Key Points:
- First model of secular change of Jovian magnetic field
- Use of magnetic field to probe Jovian internal dynamics
- Modeling of Jovian magnetic ring current variation

Correspondence to:
R. Holme,
holme@liverpool.ac.uk

Citation:
Ridley, V. A., and R. Holme (2016), Modeling the Jovian magnetic field and its secular variation using all available magnetic field observations, *J. Geophys. Res. Planets*, *121*, 309–337, doi:10.1002/2015JE004951.

Received 28 SEP 2015
Accepted 15 FEB 2016
Accepted article online 18 FEB 2016
Published online 12 MAR 2016
Corrected 14 APR 2016

This article was corrected on 14 APR 2016. See the end of the full text for details.

Modeling the Jovian magnetic field and its secular variation using all available magnetic field observations

Victoria A. Ridley[1,2] and Richard Holme[1]

[1]Department of Earth, Ocean and Ecological Sciences, University of Liverpool, Liverpool, Merseyside, UK, [2]British Geological Survey, Edinburgh, Midlothian, UK

Abstract We present new models of Jupiter's internal magnetic field and secular variation from all available direct measurements from three decades of spacecraft observation. A regularized minimum norm approach allows the creation of smooth, numerically stable models displaying a high degree of structure. External field from the magnetodisk is modeled iteratively for each orbit. Jupiter's inner magnetosphere is highly stable with time, with no evidence for variation with solar activity. We compare two spherical harmonic models, one assuming a field constant in time and a second allowing for linear time variation. Including secular variation improves data fit with fewer additional parameters than increasing field complexity. Our favored solution indicates a ~0.012% yr^{-1} increase in Jupiter's dipole magnetic moment from 1973 to 2003; this value is roughly one quarter of that for Earth. Inaccuracies in determination of the planetary reference frame cannot explain all the observed secular variation. Should more structure be allowed in the solutions, we find the northern hemispherical configuration resembles recent models based on satellite auroral footprint locations, and there is also evidence of a possible patch of reversed polar flux seen at the expected depth of the dynamo region, resembling that found at Earth and with implications for the Jovian interior. Finally, using our preferred model, we infer flow dynamics at the top of Jupiter's dynamo source. Though highly speculative, the results produce several gyres with some symmetry about the equator, similar to those seen at Earth's core-mantle boundary, suggesting motion on cylinders aligned with the rotation axis.

1. Introduction

Spacecraft missions have established the presence of large-scale magnetic fields at many of the planets in the solar system (Mercury, Jupiter, Saturn, Uranus, and Neptune, plus the Jovian moon Ganymede) and the signature of past large-scale fields for Mars and the Moon revealed by crustal remanent fields—only Venus of the major planets has not been shown to have an internal magnetic field. However, for all the planets except the Earth, models rely on limited data, for most from fleeting visits (flypasts or limited close encounters in highly eccentric orbits) which hinders magnetic field constraint in both time and space. In contrast, Earth's magnetic field is now well resolved, permitting a more detailed interpretation of decadal field changes (*secular variation*). The field generated in the core changes on multiple time scales, ranging from rapid (subyearly) jerks to full reversals on geological timescales. Such changes remain our primary probe for outer-core dynamics [e.g., *Bloxham*, 1988]. We expect active planetary fields to also undergo measurable change with time, in turn providing constraints on the internal structure and dynamics of those planets. However, there is currently no conclusive, direct observational evidence of planetary field variation, analogous to that available for the geomagnetic field.

Of the planets, Jupiter has by far the greatest time coverage of data collected, from missions from Pioneer 10 (1973) until Galileo, ending in 2003. With Juno approaching Jupiter, and planning for the JUICE mission to the Jupiter and its moons and NASA's Europa mission now well under way, it is timely to reconsider the field of Jupiter to see whether we can estimate the secular variation from current data. In this paper we remodel magnetic data collected at Jupiter in an attempt to generate more precise global representations of this field and establish whether there is observational evidence for changes with time. We build upon previous studies of jovimagnetism but note that these studies have been restricted or inconclusive for a number of reasons. Removal of fields generated external to the planet is an essential step in obtaining models for field generated within Jupiter's interior; however, this has often remained a secondary consideration. Where treatment of the

external field has been more extensive, data limitations, in number or with time, have introduced large errors to any estimates of secular variation. Furthermore, where field changes have been inferred, discrepancies in the System III 1965.0 reference frame, used in defining jovigraphic longitude, are commonly favored as an explanation, as opposed to a true variation of a magnetic source.

Here our modeling of Jupiter's magnetic field takes an alternative approach. We use measurements from all eras of near-planet exploration (1973–2003 within 12 R_J), model the external field for each orbit (to take into account possible time variability of this source), and use a minimum norm approach to create smooth models which fit the data. We first describe this approach in more detail, followed by the results gained from the magnetodisk modeling and internal field modeling. Analysis of these results allows assertions to be made about the presence of secular variation (SV). We discuss whether the results may be influenced by poor constraint of Jupiter's reference frame, as suggested by earlier studies. Finally, we consider whether there may be more structure in our models than that preferred and use the solved SV to construct maps of Jupiter's internal flow at the dynamo source, thereby placing direct constraint on Jupiter's internal dynamics.

2. Background

The magnetic field within Jupiter's magnetosphere **B** may be separated into two components: the field generated within the planetary interior (here considered below 1 atm), $\mathbf{B}_I$ and the field generated externally to the planet, $\mathbf{B}_E$. $\mathbf{B}_I$ may be represented as $\mathbf{B}_I = -\nabla\Phi$, where Φ is a scalar potential, which satisfies Laplace's equation, $\nabla^2\Phi = 0$. In planetocentric spherical coordinates (r, θ, ϕ), a general solution for this may be written as a linear combination of spherical harmonic functions,

$$\Phi = \sum_{l=1}^{\infty}\sum_{m=0}^{l}\left(\frac{a}{r}\right)^{l+1} P_l^m(\cos\theta)\left[g_l^m\cos(m\phi) + h_l^m\sin(m\phi)\right] \quad (1)$$

where a is the planetary radius, $P_l^m(\cos\theta)$ are the Schmidt quasi-normalized associated Legendre polynomials and g_l^m and h_l^m are the Gauss coefficients of degree, l, and order, m.

Despite the availability of direct magnetic field observations near Jupiter from many missions, the data are still limited in both time and space due to the spacecraft trajectories, and the inverse modeled solutions are inherently nonunique. As a consequence of the poor geographic sampling and the geometric attenuation of magnetic signal with distance from source, constraint of smaller-scale field is difficult limiting most prior jovimagnetic models to a maximum harmonic degree, l_{max}, of 3 or 4. *Connerney* [1981] demonstrated some of these issues formally, showing that even high magnitude, complex planetary field features at Jupiter's surface may not be detected if the data are sparse.

The first attempts to model Jupiter's internal magnetic field using spherical harmonic analysis were restricted to Pioneer mission data [e.g., *Acuna and Ness*, 1975, 1976] and did not model external fields within the region of data selection. We now know there to be extensive $\mathbf{B}_E$ generation within Jupiter's inner magnetosphere, of which the primary component, $\mathbf{B}_{CD}$ (CD denoting current disk), originates from an equatorial magnetodisk.

Smith et al. [1975] were the first to formally account for the presence of $\mathbf{B}_E$ in their global field models, additionally solving with external spherical harmonics to $l_{max} = 2$. However, following the return of Voyager data collected at lower latitudes and closer to the magnetodisk, a different approach was required to resolve $\mathbf{B}_I$ from $\mathbf{B}_E$. One option considered was modeling $\mathbf{B}_I$ from data collected out of the equatorial plane. This was found to exacerbate model nonuniqueness, owing to the extensive nature of the currents [*Connerney*, 1981]. Instead, comprehensive modeling of $\mathbf{B}_{CD}$ has been widely employed as the preferred method of isolating $\mathbf{B}_I$ from the observations. Examples of these models include the Euler potential approach of *Goertz* [1976], the more extensive Euler formulation of *Khurana* [1992], and the recent work of *Cowley et al.* [2008] based on the assumption of steady state, axisymmetric current systems. In this study we employ the most widely used model for $\mathbf{B}_{CD}$, devised by *Connerney et al.* [1981], which we designate as **CON1981**.

CON1981 is a six-parameter model of the magnetic field arising from an axisymmetric current disk yielding azimuthally constant current density, inversely proportional to radius from the axis, lying approximately in the planetary magnetic equator. While **CON1981** is a highly simplified representation of the true nature of Jupiter's inner to middle magnetosphere, it has repeatedly been shown to provide a good fit to the data. One example of this is the work of *Connerney* [1992], where both $\mathbf{B}_I$ and $\mathbf{B}_{CD}$ were solved for simultaneously from Voyager 1 and Pioneer 11 measurements. Using a singular value decomposition (SVD) method,

the **O6** internal field model was derived to $l_{max} = 6$; however, analysis showed only 18 of the 48 parameter vectors to be adequately resolved. The eigenvectors associated with these poorly resolved terms were subsequently removed, leaving unstable high degrees, requiring the model to be truncated at $l_{max} = 3$. While solutions are stable and are likely to return reliable elements for the low-degree part of the field, the requirement to truncate for stability means that the final model does not fit the data.

Other studies have followed the same SVD approach, for example, *Connerney et al.* [1996] in modeling data retrieved from Ulysses. This $l_{max} = 3$ solution saw effective constraint of 12 of the 15 Gauss coefficients, with the results showing similarities to previous models; however, the alternative Ulysses model of *Dougherty et al.* [1996] favored lower g_1^0. This discrepancy stems from the different approach, which sought improved fit to the data by making manual parameter changes to an **O6**+**CON1981** starting model. As will be discussed in section 5.2, the two Ulysses solutions also yielded magnetodisk properties different both from each other and from those found for Voyager 1 or Pioneer 11.

The possibility of the magnetodisk field varying with time is an important modeling consideration not accounted for by many studies which simultaneously solve $\mathbf{B}_I$ and $\mathbf{B}_{CD}$ for multiple orbits. Though the inner magnetosphere is commonly accepted to show far smaller changes with time than the outer magnetosphere, and both far smaller than Earth's magnetosphere, there is still evidence of short- and long-term temporal variation which could effect $\mathbf{B}_{CD}$. Clearly, in order to accurately model $\mathbf{B}_I$ and constrain its secular variation, it is essential to accurately account for any time variability of $\mathbf{B}_{CD}$.

The wide range of estimates quoted for jovimagnetic secular variation (JSV) can in part be attributed to these magnetodisk modeling problems. The largest and earliest JSV estimates preceded any understanding of $\mathbf{B}_E$, leading to the suggestion of a 6% decrease in the dipole magnetic moment between the Pioneer orbits of 1973 and 1974 [*Smith et al.*, 1976]. Later, *Connerney et al.* [1982] concluded that no notable variation could be detected between the octopole field modeled for Voyager 1 compared with that modeled for the Pioneer 11 encounter. This work was expanded upon by *Connerney and Acuna* [1982], being the first to coin the phrase "jovimagnetic secular variation." Fitting a linear trend to the dipole terms, they concluded any change was not statistically significant, although a rate similar to that of Earth could not be ruled out. The difference between the model g_1^0 coefficient was consistent within 1 standard deviation to an increase of 0.06% yr^{-1} or a decrease of 0.17% yr^{-1}. The equatorial dipole parameters favored a "negligible" drift of 0.22% yr^{-1}.

This equatorial drift finding was an early suggestion that any SV estimate may relate to poor constraint of the planetary rotation rate. Establishing an accurate rotation rate for Jupiter has been a longstanding problem. Unlike the terrestrial planets, Jupiter has a fluid exterior which makes it difficult to determine a frame of reference for measurement. Instead, jovigraphic longitude is based on the cyclicity of radio waves emitted from Jupiter; as the plasma emitted is directly linked to Jupiter's magnetic field via the Lorentz force, signal periodicity observed from Earth directly reflects a full rotation of the planetary interior and length of day. The International Astronomical Union System III 1965.0 period is 9 h 55 min 29.711 ± 0.04 s, corresponding to 870.536° of rotation in 24 h. Should there be inaccuracy or imprecision in this value, it is easy to understand how this may generate misleading JSV results. For example, the maximum quoted error of ±0.04 s would accumulate to a 0.445° offset in longitude over the course of 1 year.

Other studies have also noted the possibility of this reference frame drift. *Russell et al.* [2001] concluded a change in ϕ_M of 0.01° yr^{-1} between the epoch of the *Connerney* [1992] **O6** model (~1977) and the early Galileo orbits (1995–1997). *Yu et al.* [2010] later used an SVD approach to reevaluate the Galileo data, first testing for secular variation during the Galileo era only. While results were inconclusive, a secondary approach used data from 24 Galileo orbits to construct a quadrupole solution and compared this solution to models from the literature. If both this model and the **O6** model of *Connerney* [1992] are assumed to have no error, a ~0.03% yr^{-1} change in g_1^0 applies between the **O6** epoch and Galileo. Greater variation was seen in g_1^1 and h_1^1. In both tests, *Yu et al.* [2010] noted a substantial change in g_2^2 with time, but this, along with other nonaxial dipolar change, was once more attributed to inaccurate constraint of the planetary rotation rate.

In addition to direct measurements, constraint of Jupiter's magnetic configuration has been enhanced with knowledge of satellite auroral footprints. The moons produce particles which become ionized and so charged and then move along field lines to generate aurora. Using the **O6** model in conjunction with 112 images of the Io footprint from the Hubble Space Telescope (HST) and NASA's Infrared Telescope Facility, *Connerney et al.* [1998] created the partially solved $l_{max} = 4$**VIP4** model. This model, and its successor **VIT4**, better constrains

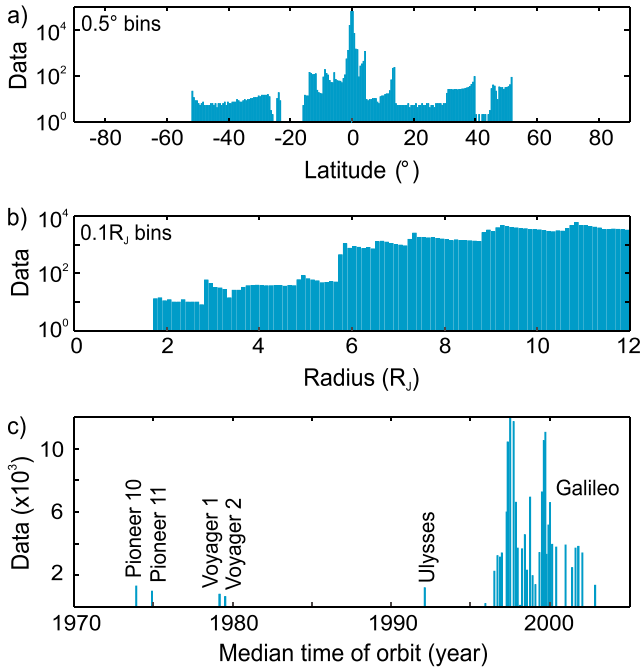

Figure 1. Distribution of full data set with (a) jovigraphic latitude, (b) radial distance from Jupiter, and (c) time.

the polar field configuration, especially in the south where there is a dearth of spacecraft magnetometer data. *Grodent et al.* [2008] extended this approach by studying over 1000 HST images of the Io, Ganymede, and Europa footprint locations. *Hess et al.* [2011] used the extended eigenvectors of the VIP4 model to construct a more detailed full spherical harmonic solution, **VIPAL**, using a more accurate footprint mapping approach in combination with limited spacecraft data. While we do not use auroral information, we demonstrate that similar field structures can be derived from satellite data alone.

3. Data

The data employed in this study have been selected from that collected by all spacecraft within 12 R_J of Jupiter (where 1 R_J is taken as 71,492 km, the equatorial radius). This radial limit was placed on the data selection to minimize external field contamination. The criterion is met by measurements from five flyby missions of Jupiter (Pioneer 10 and 11 (1973 and 1974), Voyager 1 and 2 (1979), and Ulysses (1992)) and data from 34 passes of the planet by the Galileo orbiter between ~1995 and 2003. For simplicity, in this study we avoid the use of traditional target body naming convention for the Galileo orbits and instead make use of the mission name and orbit number (for example, Pioneer 11 = *P11* and Galileo Orbit, Callisto 3 = *G03*).

For each pass of the planet, measurements collected with proximity to the moons were manually picked and removed prior to modeling in order to avoid contamination from sources such as Ganymede's dynamo and Europa's induced field. Of the Galileo passes *G05* occurred during solar conjunction, and consequently, no data are available; data at low perijove from *G34* and all of *G35* (the final orbit) were discarded owing to the presence of periodic noise in the magnetometer measurements; and data are limited from the orbital insertion period of *G00* and *G13* which occurred predominantly during solar conjunction. The perijove of *P11* also occurred during conjunction, and so orientation of data are not available; these data are not used.

Figure 1 demonstrates the distribution of all data by latitude, radius, and time. A summary of the data properties is presented in Table 1. There are several notable features. Over 96% of observations were collected at latitudes of ±2.5°, with no data collected at > ±455°. Furthermore, only ≃1% of the data were collected at > ±20° with only *P11* and Ulysses (*ULY*) venturing to greater latitudes within 12 R_J. Radial data distribution is also poor. Of all 39 orbits, the only passes within 5 R_J of the planet were made by Pioneer 10, Pioneer 11, Voyager 1, and Galileo 34, accounting for just 0.6% of the observations. Finally, there is clearly an imbalance in the temporal distribution of data collection: Galileo dominates accounting for ~97% of the total data.

Table 1. Summary of Magnetometer Data Employed in This Study

Mission	Year(s)	Orbits	Magnetometer Type	Sampling Rate (Hz)	Averaged Data (s)	Operating Range Error (nT)	Error Employed (nT)
P10	1973	1	VHM	$5\frac{1}{3}$	60	85.93	0.859
P11	1974	1	VHM	$5\frac{1}{3}$	60	85.93	0.859
VY1	1979	1	FGM	$16\frac{2}{3}$	12	0.513	0.513
VY2	1979	1	FGM	$16\frac{2}{3}$	12	0.513	0.513
ULY	1992	1	FGM	$<\frac{1}{2}$	60	21.5	0.215
GAL	1995–2002	36	FGM	3	24	0.032	0.960

The uncertainty associated with each measurement is dependent on factors including instrumental error and drift, attitude, observation digitization, and data storage capability. The instrumental errors for the primary magnetometer operating ranges are listed in Table 1 and were considered in construction of the data error covariance matrices, as discussed in the next section. We also corrected the Galileo data with a uniform orthogonal gain correction of 0.9911, as first suggested by *Yu et al.* [2010]. With this correction, our $\mathbf{B}_I$ models show a clear reduction in data misfit, and thus, applying the correction minimizes the estimate of secular variation, improving our confidence that any secular variation observed is required by the data.

4. Method

We take an iterative approach to modeling $\mathbf{B}_I$ and $\mathbf{B}_{CD}$, the latter being solved individually for data from each orbit, in order to allow time variability of the external field. First, the residual between the **O6** model of *Connerney et al.* [1996] and one orbit of data is calculated. Assuming this residual to be dominated by the external field, we then calculate the best fitting **CON1981** magnetodisk model, as described in detail in the next section. The modeled $\mathbf{B}_{CD}$ is then removed from the original data set. Having executed this for all orbits, the data are recompiled and new spherical harmonic models of $\mathbf{B}_I$ are generated. The procedure is then iterated.

4.1. The Regularized Minimum Norm Approach

In a further significant departure from previous studies of Jupiter's main field, we follow a regularized minimum norm approach. We seek solutions for $\mathbf{B}_I$ which fit the data but are also smooth and thus display physically plausible characteristics. Using this approach alleviates the problems associated with using finite, sparse data to create finite models of intrinsically infinite, physically complex systems. Regularization acts to eliminate unresolved parameter vectors in the method, creating solutions with stable higher-degree harmonics. *Shure et al.* [1982] first applied regularization to model the geomagnetic field. Since then, the approach has been applied to other planets where there are limited data such as Mercury [*Uno et al.*, 2009] and Saturn [*Sterenborg and Bloxham*, 2010]. Our methodology closely follows of that employed by *Holme and Bloxham* [1996], where the regularized minimum norm approach was used to model the magnetic fields of Uranus and Neptune from single flybys by Voyager 2. We refer the reader to this work for a more complete overview of the topic and our chosen smoothing norm.

Solving for $\mathbf{B}_I$ from the data is a linear inverse problem,

$$\boldsymbol{\gamma} = \mathbf{A}\mathbf{m} + \mathbf{e} \tag{2}$$

where $\boldsymbol{\gamma}$ is a vector containing the data, $\mathbf{m}$ is the model vector containing the Gauss coefficients to be determined, from equation (1), $\mathbf{A}$ is a matrix containing the equations of condition which link $\mathbf{m}$ and $\boldsymbol{\gamma}$, and $\mathbf{e}$ is the error vector. To obtain our solution, we construct the generalized inverse, to minimize an objective function comprising squared misfit to data and a measure of roughness

$$Q = (\boldsymbol{\gamma} - \mathbf{A}\mathbf{m})^T \mathbf{C}_e^{-1} (\boldsymbol{\gamma} - \mathbf{A}\mathbf{m}) + \lambda \mathbf{m}\boldsymbol{\Lambda}\mathbf{m} \tag{3}$$

where $\mathbf{C}_e^{-1}$ is the data-error covariance matrix, $\boldsymbol{\gamma}$ is a *Lagrange multiplier*, referred to as the damping parameter, controlling the strength of the smoothing norm defined by the matrix $\boldsymbol{\Gamma}$.

4.2. Choice of Smoothing Norm

The simplest choice of smoothing norm is the identity matrix, leading to minimization of the sum of squares of the parameters; however, it can also represent a more complex physical constraint. Numerous smoothing

norms were considered with similar results, but the best trade-off between misfit and complexity was found from following the approach of *Holme and Bloxham* [1996]. This is derived from the formalism of *Gubbins* [1975] which places a lower bound on ohmic heating, J, originating in a planetary dynamo of known volume, V, and constant conductivity, α, minimizing

$$\int \frac{J^2}{\alpha} \mathrm{d}V\Big|_{r<R_\alpha} \tag{4}$$

The conducting region is assumed to have a constant conductivity for metalic hydrogen, with radius R_{IMT} (IMT = insulator-metal transition), above which ionic conductivity is assumed to fall off linearly to zero at an outer radius R_α. This leads to a diagonal matrix with elements

$$\frac{(l+1)(2l+1)(2l+3)(2l+4)\left[R_\alpha - R_{\mathrm{IMT}}\right]}{4\pi\alpha_0 l\left[\left(R_\alpha\right)^{(2l+4)} - \left(R_{\mathrm{IMT}}\right)^{(2l+4)}\right]} \tag{5}$$

Our current understanding of Jupiter's interior structure is limited but has advanced in recent years with high-pressure experimental studies; more advanced and relevant hydrogen-based equations of state; and improved computational models [e.g., *Guillot*, 1999; *Nettelmann et al.*, 2008]. At the most basic level, is simply the question of where Jupiter's dynamo originates, but there is also uncertainty surrounding the nature of the insulating molecular hydrogen to conductive, metallic hydrogen transition: Is this transition to the dynamo abrupt and discrete, like the Earth's core-mantle boundary, or is it continuous?

The models we present employ $R_{\mathrm{IMT}} = 0.85R_J$ and $R_\alpha = 0.90R_J$. These depths have been chosen based on several factors. The largest influence on our decision was the results from shock compression experiments [e.g., *Nellis et al.*, 1995; *Weir et al.*, 1996]. These produced metallic hydrogen at 140 GPa and 3000 K, via a mechanism suggesting continuous molecular dissociation and a continuous phase transition at Jupiter. *Nellis et al.* [1996] used these values to favor $R_{\mathrm{IMT}} = 0.90R_J$, while *Nellis* [2000] conclude $R_\alpha = 0.95R_J$, as this is the depth which corresponds to a conductivity which is commonly attributed to magnetic field generation in the ice giants Uranus and Neptune.

We investigate these quoted transitions. By comparing them with recent theoretical models for the Jovian interior [e.g., *Guillot*, 1999; *Nettelmann et al.*, 2008], we find the given pressures correspond to $R_{\mathrm{IMT}} \simeq 0.835R_J$ and $R_\alpha \simeq 0.875R_J$ not those quoted previously. We do note that (a) the temperatures reached experimentally do not approach those modeled theoretically at matching pressures and (b) the presence and greater atomic temperature of helium is also likely to raise the local temperature, relative to a planetary interior composed of pure hydrogen [*Nellis et al.*, 1996]. Taking these factors into consideration, a choice of $R_{\mathrm{IMT}} = 0.85R_J$ and $R_\alpha = 0.90R_J$ appears appropriate.

Further a posteriori justification for these values comes with analysis of the magnetic spectra of our main field models, which may in themselves constrain the dynamo source depth. *Lowes* [1974] defined a geomagnetic power spectrum, separating the mean square field as a function of degree

$$P(l,r) = (l+1)\left(\frac{a}{r}\right)^{(2l+4)} \sum_m \left(g_l^{m2} + h_l^{m2}\right) \qquad \oint \mathbf{B}^2 \mathrm{d}\Omega = \sum_l P(l,r) \tag{6}$$

and identified that the geomagnetic power spectrum $P(l)$ for $2 \leq l \leq 14$ becomes white when plotted at the core-mantle boundary. An early study by *Elphic and Russell* [1978] applied this logic to $l = 3$ models of Jupiter's field derived from Pioneer observations; however, the results were inconclusive. Our models display a degree of flattening at $R_{\mathrm{IMT}} = 0.85R_J$ and $R_\alpha = 0.90R_J$ (section 6.1), consistent with our assumptions.

To minimize our objective function (equation (3)), we also require information about the data errors for construction of $\mathbf{C_e^{-1}}$. We employ the values listed in the final column of Table 1, as opposed to the quoted error associated with the primary magnetometer operating range. These values were chosen following analysis and a posteriori confirmation of consistency with the fit to the data. Making these changes informally weights the inversion away from the extensive Galileo data set, crudely compensating for the relative lack of earlier measurements. Furthermore, applying the same error for all measurements from one orbit places more confidence in the higher magnitude observations collected closer to the planet.

From the objective function (equation (3)), we use Cholesky decomposition to find our maximum likelihood solution, $\hat{\mathbf{m}}$,

$$\hat{\mathbf{m}} = \left(\mathbf{A^T C_e}^{-1} A + \lambda\Lambda\right)^{-1} \mathbf{A^T C_e}^{-1} \gamma \tag{7}$$

This is executed for numerous λ values, allowing a trade-off curve between solution norm and model-to-data residual to be plotted. Models with λ values found in the trade-off curve knee are optimal, as they are smooth (physically plausible) while also minimizing misfit to the observations. With ill-posed problems such as this, it is common to encounter a broad knee region and choosing a favored model is highly subjective. To overcome this, further analysis of the solution properties, such as the magnetic power spectrum, surface field plots, and model resolution, was undertaken prior to finalizing the choice of damped model. The process was then iterated: the difference between the new damped model of $\mathbf{B}_I$ and each orbit of data was calculated and used for input to model $\mathbf{B}_{CD}$, with the full procedure repeated until convergence on both the magnetodisk parameters and $\mathbf{B}_I$.

4.3. Constraining Jovimagnetic Secular Variation

Using the data set compiled at the final iteration, we present two models of $\mathbf{B}_I$:

1. **JCF** models (*Jupiter constant field*) assume that the field is unchanged during the 1973–2002 period of investigation. The total number of parameters are $l_{\max}(l_{\max}+2)$ Gauss coefficients, g_l^m, defined in nanotesla.
2. **JSV** models (*Jupiter secular variation*) allow linear time variation of the Jovian field by additionally parameterizing each Gauss coefficient by a temporal parameter,

$$g_l^m(t) = g_l^m{}_0 + \dot{g}_l^m t \tag{8}$$

where $\dot{g}_l^m$ is the secular variation (nT yr^{-1}) and $g_l^m{}_0$ is the resulting magnitude of g_l^m at time $t = 0$, set halfway through the period of observations at 1988.38. The total number of parameters in these models is double that of **JCF**, as each Gauss coefficient has a corresponding SV coefficient. We also introduce a further damping parameter, τ, to minimize the SV in our **JSV** objective function, so that equation (3) becomes

$$Q = (\boldsymbol{\gamma} - \mathbf{Am})^{\mathbf{T}}\mathbf{C_e}^{-1}(\boldsymbol{\gamma} - \mathbf{Am}) + \lambda\mathbf{m_s}\Lambda\mathbf{m_s} + \tau\mathbf{m_t}\Lambda\mathbf{m_t} \tag{9}$$

where $\mathbf{m_s}$ are the Gauss coefficients and $\mathbf{m_t}$ are the temporal coefficients. In regularizing the model in time we employ the same $\boldsymbol{\Lambda}$.

Through inspection of the resulting **JCF** and **JSV** models for optimal properties, such as smoothness, misfit to data, and resolution, we can investigate whether the spacecraft measurements provide evidence for secular variation of Jupiter's field. We note that these improvements must be substantial for SV to be inferred: simply by increasing the number of free parameters for the **JSV** solutions, a better fit to data is inevitable.

5. Modeling and Removal of the Magnetodisk Field

Having established the residual between a model for $\mathbf{B}_I$ and one orbit, we use the **CON1981** model to solve Jupiter's magnetodisk field, $\mathbf{B}_{CD}$. Allowing as much variability in this component as possible (certainly from orbit to orbit) is important to prevent external field variations being aliased into our models of internal field secular variation. Contributions to inner magnetospheric **B** from other sources of $\mathbf{B}_E$ are favored to be orders of magnitude less than either $\mathbf{B}_I$ or $\mathbf{B}_{CD}$ [*Engle*, 1991].

5.1. Methodology

The field is described with a vector potential in cylindrical coordinates, (ρ, ϕ, z), with z parallel to the planetary dipole axis and ρ and ϕ in the magnetic dipole equator. An axisymmetric disk yielding components of $\mathbf{B}_{CD}$ in B_z and B_ρ is defined using just six parameters: inner and outer edges, R_0 and R_1; half thickness, D; the disk orientation relative to Jupiter's rotation axis in colatitude, θ_{CD}, and relative to the System III 1965.0 reference frame in longitude, ϕ_{CD}; and a parameter $(\mu_0 I_0)/2$ defining the strength of the field generating currents, assumed to flow only azimuthally, with the current density falling off as the inverse of cylindrical radius. A good fit to the Voyager 1 data was found by *Connerney et al.* [1981] when this disk was bound at $R_0 = 5R_J$ near Io's orbit, $R_1 = 50R_J$ and $D = 2.5R_J$, with $(\mu_0 I_0)/2 = 225$ and orientated with the planetary dipole magnetic equator at $\theta_{\mathrm{CD}} = 9.6°$ and $\phi_{\mathrm{CD}} = 158°$. *Connerney et al.* [1981] use infinite integrals of Bessel functions to obtain the field values; we implement the restatement of this result of *Giampieri and Dougherty* [2004] which reposes these as closed form summations. The resulting calculations are computationally easier and less time consuming, allowing easier exploration of disk parameter space.

5.2. The True Nature of Jupiter's Inner Magnetosphere

Our preference to solve $\mathbf{B}_{CD}$ using **CON1981** relates to its proven ability to model the magnetodisk field and the fact that more complex solutions for $\mathbf{B}_{CD}$ have similar configurations within the inner magnetosphere

[e.g., *Khurana*, 1992]. However, modeling this complex phenomenon as a simple disk has its pitfalls and there are several places where **CON1981** cannot capture the true nature of the region.

In reality, the inner magnetospheric plasma environment changes with radius. From the cold inner torus (5–5.2 R_J), through the ribbon (5.2–5.9 R_J), to the warm outer torus (5.9–10 R_J) there are observed differences in ion and electron densities which are not taken into account by the constant current strength of **CON1981**. These changes accompany an increase in plasma dispersion toward Io [*Bagenal*, 1994], again not accounted for by the constant D of the magnetodisk model. Dusk-dawn asymmetries in the magnetodisk field [e.g., *Bunce and Cowley*, 2001; *Connerney*, 1981] and the ribbon region [e.g., *Sandel and Broadfoot*, 1982] have also been noted, alongside variations linked to longitudinal asymmetries in the planetary field [e.g., *Dessler and Sandel*, 1992]. There is also evidence for disk corotation breakdown within 2 R_J of Io (up to ~5% from rigid) and gradually outward of Io's orbit (~1–10% from 6–10 R_J) [e.g., *Pontius*, 1995]. Disk tilt also varies with radius in the inner magnetosphere, with the less energetic cold torus particles aligning closer to the centrifugal equator, $\theta_{CS} \simeq 6.4^\circ$, while by 10–15 R_J the warmer plasma has been shown to lie closer to the magnetic dipole equator, θ_M.

There are also changes in the configuration which occur with different time scales. This reinforces the need to model $\mathbf{B}_{CD}$ for each orbit but even this may not be adequate to fully resolve short-term changes. With the exception of current strength, *Connerney et al.* [1981] found an identical magnetodisk configuration can adequately fit the Voyager 1, Voyager 2, and Pioneer 10 observations; however, different configurations for inbound and outbound passes were also preferred, suggesting a possible dayside magnetodisk thickening asymmetry as previously noted. Analysis of Ulysses measurements by *Balogh et al.* [1992] found a similar discrepancy, with the inbound pass requiring a ~ 45% reduction in the current strength parameter relative to the **CON1981** Voyager 1 values. This configuration for Ulysses is broadly consistent with *Dougherty et al.* [1996], which favors lower $\mu_0 I/2 = 100$ but increased $D = 4R_J$, while *Connerney et al.* [1996] prefers an alternative Ulysses configuration of $R_0 = 7.1R_J$, $D = 3.3R_J$, $\mu_0 I/2 = 185$, $\theta_{CD} = 6.5^\circ$, and ϕ_{CD}=154°.

Other evidence for short-term changes to the inner magnetosphere also exists. *Frank and Paterson* [2001] and *Thomas et al.* [2004] note discrepancies at 6–7 R_J in electron density of up to a factor of 3 between individual Galileo orbits and between Galileo orbits and a Voyager observation-based model [*Bagenal*, 1994]. Spacecraft have also measured large-scale plasma injections, with multiple occurrences daily and occasional clustering in time [*Krupp et al.*, 2004]. During these events, material in the Io plasma torus from beyond $\simeq 9R_J$ is transported radially by up to several R_J toward Jupiter, over a narrow azimuthal range (30–40°).

Longer-term trends include a 2 month period identified by *Brown and Bouchez* [1997], during which spectrographic techniques identified the plasma torus mass increasing by up to 30%. Initiation of a new volcanic plume at Io was hypothesized as a possible cause for this increase, compensated for by increased plasma outflow into the middle magnetosphere. Whether inner magnetospheric $\mathbf{B}_{CD}$ might be influenced by changes to the solar wind remains a matter for debate. A correlation between inner radiation belt emission/flux density and solar wind ram pressure has been noted, occurring with a ≃2 year time lag [*Bolton et al.*, 1989; *Klein et al.*, 2001].

5.3. Approach

Unlike solving $\mathbf{B}_I$, solving $\mathbf{B}_{CD}$ is a nonlinear problem and there are many disk configurations which can fit the data from one orbit. The result is a rough function landscape with many local minima. Finding the global minimum is difficult; strong parameter covariance and instability leads to many solutions with implausible disk configurations. To counter this, the data were forward modeled, cyclically varying each disk parameter through a range of physically realistic values. Initial conditions were set to those favored by *Connerney et al.* [1981] for Voyager 1 and then solved in turn: (a) current strength, $\mu_0 I/2$; (b) simultaneously for orientation parameters θ_{CD} and ϕ_{CD}; and (c) simultaneously for R_0 and D (routine *C-O-RD*). This order was chosen based on preliminary tests, computation time, and perceived ability for the parameters to influence field configuration/differ significantly from that stated by *Connerney et al.* [1981]. The constraints placed on the minimum and maximum parameter values are given in Table 2. With data only being used from within 12 R_J, R_1 is poorly constrained; we fixed this at 50 R_J. We further were unable to resolve R_0 in many cases, as most orbits were still far from this boundary even at closest approach. Furthermore, as with the model **CON1981** data from within 5 R_J were also removed prior to solving (although reconsidered for further internal field modeling) to ensure that the magnetodisk solution was not biased by unmodeled high-degree internal field unaccounted for by the $\mathbf{B}_I$ model.

Table 2. Favored Magnetodisk Parameters Retrieved From Two Alternative Solving Routines for Orbit *G23*[a]

Parameter	Routine Minimum	Routine Maximum	*C-O-RD*	*CD-O-R*
R_0 (R_J)	4.004	7.996	4.004 UR	4.252
D (R_J)	1.35	3.65	2.831	3.262
$\mu_0 I_0/2$	70.0	330.0	164.6	143.0
θ_{CD} (°)	0.0	18.0	8.16	9.30
ϕ_{CD} (°)	100.0	240.0	160.24	160.34

[a]UR signifies unresolved.

Despite optimizing our approach, small changes to our *C-O-RD* routine were still capable of causing significant changes in preferred magnetodisk configuration, highlighting the strong nonlinearity. To demonstrate this, Figure 2 compares the fit to the *G23* data in spherical coordinates, using our preferred solving routine, *C-O-RD*, and an alternative, *CD-O-R*, which uses the same initial conditions but solves in turn: (a) $\mu_0 I/2$ and D simultaneously, (b) disk orientation, and (c) R_0 before iterating the cycle. The resulting magnetodisk configurations found from this preferred fit are listed in Table 2.

There is little difference between the fit to the data gained using each routine; the modeled field in the $\mathbf{B}_\theta$ and $\mathbf{B}_r$ directions are almost identical, while the smallest component, in the $\mathbf{B}_\phi$ direction, shows a marginally better fit for *C-O-RD*. However, the disk configurations producing the field differ substantially: a difference of 0.43 R_J exists between D; $(\mu_0 I_0)/2$ is 15% higher for *C-O-RD*; and θ_{CD} differs by over 1°. However, the product of $\mu_0 I_0/2$ and D, a measure of the total magnitude of the current disk, is 465.98 for *C-O-RD* and 466.47 for *CD-O-R*, confirming a strong covariance between these parameters, previously identified by *Connerney et al.* [1982]. To further explore this covariance, the disk field was forward modeled for a range of D, $\mu_0 I_0/2$, and θ_{CD} and the corresponding fit to data from different orbits was examined; R_0, R_1, and ϕ_{CD} were kept constant at the *Connerney et al.* [1981] preferred values. In doing so, a striking correlation can be demonstrated between θ_{CD}, $D\mu_0 I_0/2$ and the model-data residual. Figure 3 shows this correlation for orbit *G23*, where a distinct reduction in total RMS misfit is seen for certain values of $D\mu_0 I_0/2$. Similar results are obtained for other orbits.

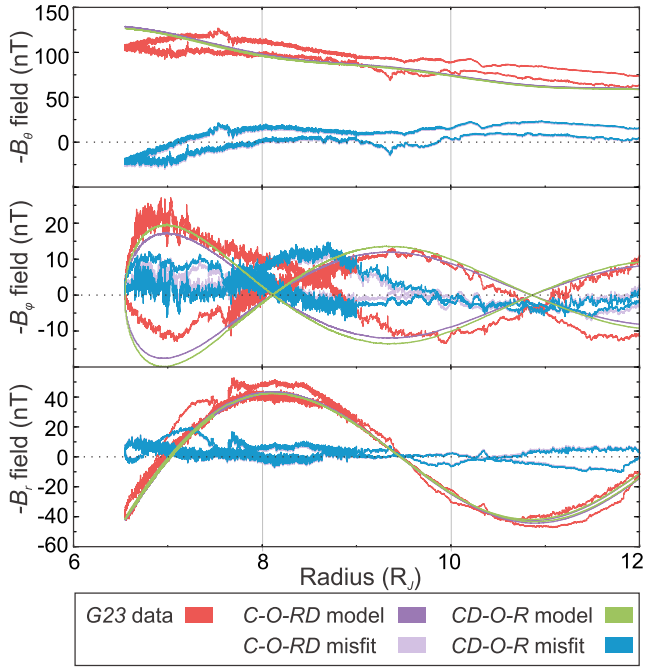

Figure 2. Fit to *G23* data achieved using two different routines with alternative parameter solving order. Corresponding resolved parameters listed in Table 2.

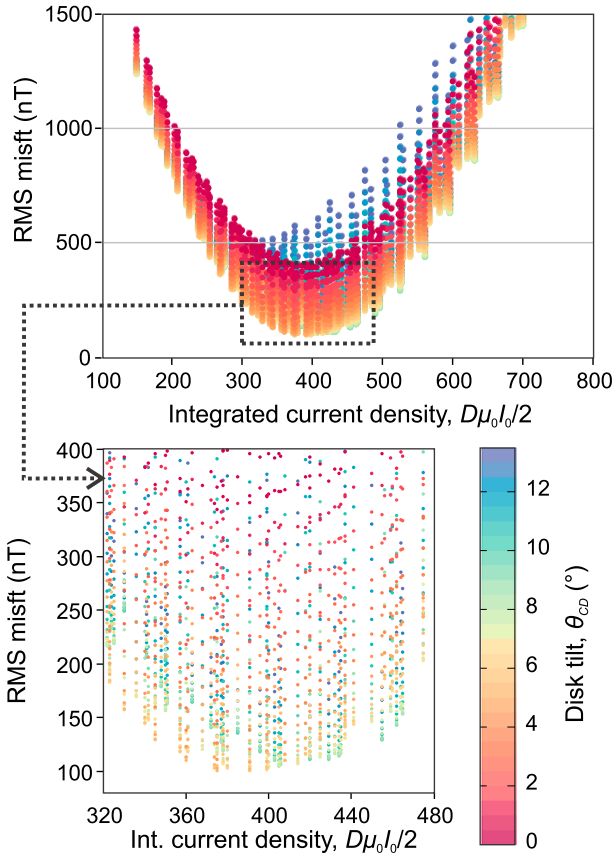

Figure 3. Root-mean-square (RMS) misfit as a function of $D\mu_0 I_0/2$ and θ_{CD} for orbit *G23*. (bottom) Minimum in higher resolution.

The models in the range of the *G23* minimum possess $\theta_{CD} < 7°$, lower than that favored by *Connerney et al.* [1981]. Most well-resolved orbits also show this preferentially reduced θ_{CD}. This may reflect the true nature of the inner magnetosphere: the less energetic particles of the cold Io torus align closer to the centrifugal equator, $\theta_{CS} \simeq 6.4°$, while by 10–15 R_J the warmer plasma lies closer to the magnetic dipole equator, $\theta_M \simeq 9.8°$.

5.4. Disk Modeling Results

Figure 4 presents the final disk parameters resolved for each orbit of data after 14 $\mathbf{B}_I - \mathbf{B}_{CD}$ iterations using the *C-O-RD* routine; the last plot shows the corresponding root-mean-square (RMS) misfit between the resulting model and the input data.

The majority of orbits yield plausible disk configurations, settling on parameter values well within the constraints employed, with the exception of R_0, which as expected was generally poorly resolved. Of the orbits which displayed abnormalities in one or more parameters, θ_{CD} of both Voyager disk models reached greater angles than θ_M; *G00*, *G13*, and *G34* showed low $\mu_0 I_0/2$ and/or high ϕ_{CD}, probably due to the limitations in data coverage described in section 3; and *P11* showed a particularly low θ_{CD}, likely related to the high-latitude trajectory, in regions of low $\mathbf{B}_{CD}$. These issues are reflected in the associated RMS misfit values.

Considering only the well-resolved orbits, θ_{CD} tends to lie below 9.8°, following the reasoning of the θ_{CS}-θ_M transition in this region. Variation in ϕ_{CD} is as expected, generally around or less than the planetary dipole longitude, likely related to localized regions of corotation breakdown. With few exceptions, *D* is larger than the 2.5 R_J suggested by *Connerney et al.* [1981], ranging broadly between 2.7 and 3.1 R_J; complementing this, the disk current density parameter consistently displays a significantly smaller magnitude than the *Connerney et al.* [1981] Voyager 1 preferred magnitude. This reflects the strong parameter covariance previously discussed.

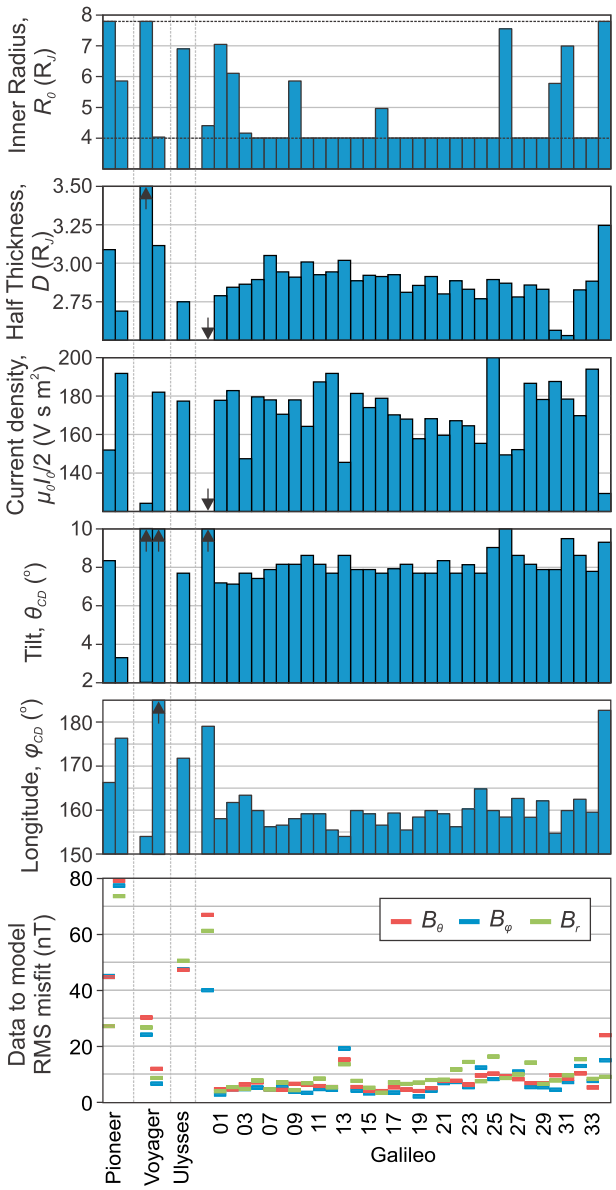

Figure 4. CON1981 magnetodisk parameters for each orbit, in chronological order, solved using the *C-O-R-D* approach. Dashed lines in R_0 plot show upper and lower constraint placed on these values by the routine; arrows show where the solved parameters are outside the plotted range.

Our results favor a stable inner magnetospheric environment on the large scale; however, the simplistic configuration of **CON1981** is clearly influential in reaching this conclusion. Trends were explored between individual parameters and orbital position in time and space (e.g., with perijove and satellite proximity), but no clear relationships were found. Owing to the strong covariance, we favor that changes to $D\mu_0 I_0/2$ may be more useful in characterizing magnetodisk variation than any individual parameter.

No clear spatial relationship could be identified in $D\mu_0 I_0/2$, but there is evidence of time variation. Figure 5 plots $D\mu_0 I_0/2$ for orbits during the Galileo epoch. Excluding the orbits with parameter abnormalities, a trend appears, with two periods of $(D\mu_0 I_0)/2$ decrease, one ending around 2000 and the other during the latter part of the Galileo mission. Alongside this, both the concurrent and 2 year displaced sunspot number are overlain, the latter being chosen following the observed lag in correlation between inner radiation belt emission/flux density and solar wind ram pressure [*Bolton et al.*, 1989; *Klein et al.*, 2001]. No clear relationship between $(D\mu_0 I_0)/2$ and solar activity can be identified, suggesting that these trends relate to changes

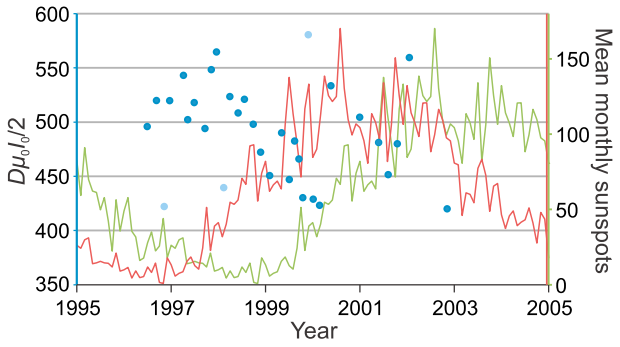

Figure 5. Dark blue markers show $D\mu_0 I_0/2$ during the Galileo period for *C-O-R-D* routine solved disk configuration. Light blue markers signify orbits with one or more distinctly abnormal magnetodisk parameters: *G03*, *G13*, and *G25*. Concurrent and 2 year offset sunspot number shown in red and green, respectively.

internal to the Jovian magnetosphere. *Russell and Kivelson* [2001] noted ~4 times greater rate of ion production at Io at the start of the Galileo missions than by orbits **G24**-**G27**. Our calculated $(D\mu_0 I_0)/2$ values may reflect this observation.

Our consideration of the range of possible disk parameters has been of great importance to interpretation of possible secular variation. We argue below for evidence of possible change in the internal magnetic field; before we make such an argument, it has been important to allow sufficient variation in the external field that it can be ruled out as a source of this change. It is important to note that uncertainty in the disk parameters due to covariance has no impact on our primary goal, the modeling of the internal planetary field. This covariance arises precisely because such changes do not impact on the field predicted by the model. The current disk is calculated to remove bias from external field, and this is achieved even if individual disk parameters cannot be resolved. Nevertheless, insights from this work on the correlation between different features in the disk have the potential to usefully inform future modeling of the innermost magnetosphere of Jupiter, especially from the Juno mission.

6. Main Field Modeling: Results and Analysis

Having reached $\mathbf{B}_{CD}$ and $\mathbf{B}_I$ model convergence, models were compared for both constant field (**JCF**) and constant secular variation (**JSV**). A truncation of $l_{max} = 7$ was found to be sufficient that the solutions were constrained by the regularization and not the choice of truncation.

6.1. Comparison of JCF and JSV Models

We present three solutions of our time constant field models, **JCF**, and three solutions of our time varying field models, **JSV**. The **JCF** solutions all lie in the broad knee region of the objective function misfit-norm trade-off curve but possess slightly different damping magnitudes. This is illustrated by the colored points on the thick black curve in Figure 6b. The levels of damping translate to a solution with smoother field ($\lambda = 7 \times 10^{-1}$); a solution with intermediate complexity ($\lambda = 2 \times 10^{-1}$); and a more structured solution ($\lambda = 1 \times 10^{-1}$). Note that these values lack easy interpretation, but their relative magnitudes give an indication of the relative influence of the damping.

Alongside these we present three **JSV** solutions which retain identical field smoothing λ but now allow linear temporal change, damped by τ. Our complementary **JSV** solutions are smoother field with SV ($\lambda = 7 \times 10^{-1}$, $\tau = 2 \times 10^3$); intermediate field complexity with SV ($\lambda = 2 \times 10^{-1}$, $\tau = 7 \times 10^3$); and structured field with SV ($\lambda = 1 \times 10^{-1}$, $\tau = 2 \times 10^4$). Justification for our choice of these τ values follows, though we favor the intermediate smoothed solutions and give priority to these in our discussion.

The solid black line in Figure 6b is the **JCF** trade-off curve. The dotted colored lines breaking away from this show how field smoothness and data misfit change when the same level of λ is retained, but solving employs the **JSV** approach with temporal changes damped by varying τ. As expected, with high τ, temporal changes were fully smoothed out and the field approximated the complementary **JCF** solution. Decreasing τ allows spatially more complex secular variation, removing structure from the modeled field and smoothing it (reduced norm). At the same time, there is a notable reduction in the misfit to the data compared to the complementary **JCF** solutions. With further lowering of τ, a knee is reached in the **JSV** trade-off curves.

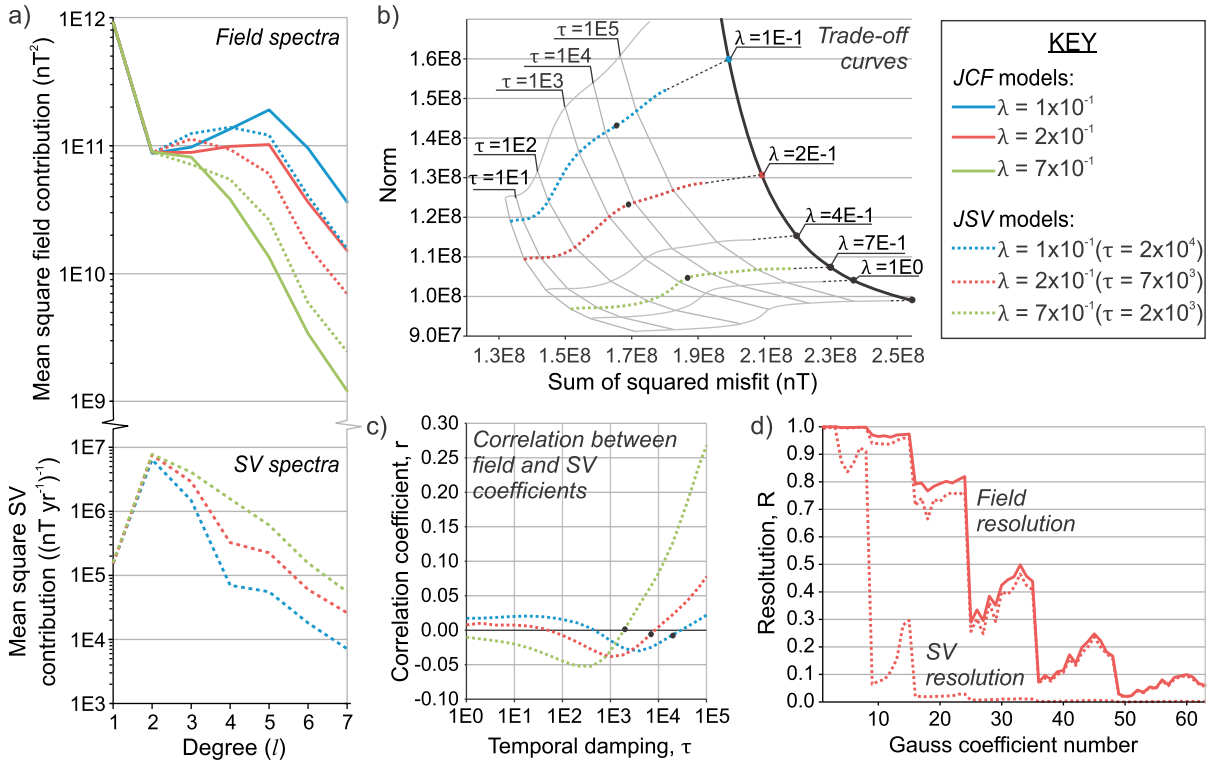

Figure 6. Comparison of preferred **JCF** and **JSV** modeling results: (a) lowes power spectra and corresponding **JSV** model SV spectra; (b) trade-off curves for model-to-data misfit and modeled field norm; (c) correlation between **JSV** model Gauss coefficients and conjugate linear SV coefficients; (d) comparison of coefficient resolution for **JCF** $\lambda = 2 \times 10^{-1}$ model and **JSV** $\lambda = 2 \times 10^{-1}$, $\tau = 7 \times 10^3$ model. Coefficients ordered from g_l^m to h_l^m with increasing l and m (so, e.g., $(g_2^0, g_2^1, h_2^1, g_2^2,$ and $h_2^2)$, not $(g_2^0, g_2^1, g_2^2, h_2^1,$ and $h_2^2)$).

Lowering τ beyond this knee allows unrealistically complex and high-magnitude temporal changes which are not required by the data. As a consequence, our favored levels of τ lie close to this knee, as indicated by the black circles in Figure 6b.

The model coefficients for our preferred solutions are given in Table 3, and maps of their B_r and the total modeled change in B_r are given in Figure 7, projected onto Jupiter's ellipsoidal surface (ellipticity 0.065). Our modeled field is strongly dipolar and B_r generally shows similar, but smoother structure when temporal change is permitted; however, there are other notable differences. All the **JSV** solutions possess a greater maximum field magnitude at the north pole. For example, the model with intermediate λ has a maximum B_r of 15.89 G, while that of the intermediate λ**JSV** solution is 16.70 G. In contrast, each **JSV**-**JCF** pair agree on the southern hemisphere maximum magnitude to within 0.2 G. The southern polar field magnitude is also significantly less than the north; for the intermediate λ**JCF** and **JSV** models, the maximum magnitude is −11.11 G and −11.28 G, respectively. The largest difference in field structure for each model pair is found around $\theta \simeq 70°$, $\phi \simeq 290°$, where lower λ**JCF** solutions favor an area of negative flux, not present in the **JSV** solutions. The modeled change in B_r accompanying the **JSV** field is strongly quadrupolar, and, though higher λ damped models show increasingly complex temporal changes, they are all of the same order of magnitude for the preferred solutions.

The model differences are also reflected in the power spectra of Figure 6a, with both the field and SV contribution displayed. There is good agreement between the dipole and quadrupole contributions from both approaches and for all damping levels; however, divergence is seen above $l = 2$ where damping-dependent flattening occurs to varying degrees. A distinct dropoff in field power is observed beyond $l = 5$ for the strong/intermediate λ damped models and beyond $l = 3$ for the weak λ damping. The mean square SV power is dominated by the quadrupole and octopole, confirming that seen in the **JSV** B_r field maps.

A further qualitative study was carried out to ascertain which combination of λ, R_{IMT} and conductivity dropoff produced the flattest main field spectra. The results favored λ between our structured and intermediate

Table 3. Coefficients for Preferred $\lambda = 2 \times 10^{-1}$ Models: **JCF**($\psi = 0.0°$) Gauss Coefficients; **JSV**($\psi = 0.0°$) Gauss and Temporal Coefficients; and **JSV**($\psi = -3.8°$) Gauss and Temporal Coefficients[a]

l	m	g_l^m	h_l^m	g_l^m	h_l^m	$\dot{g}_l^m$	$\dot{h}_l^m$	g_l^m	h_l^m	$\dot{g}_l^m$	$\dot{h}_l^m$
1	0	409859.45		409620.37		43.78		409586.87		44.74	
1	1	−68670.56	23707.03	−68257.07	23845.92	−101.86	−128.10	−67423.60	26092.85	−45.54	28.41
2	0	10399.59		14194.39		433.41		14260.01		445.14	
2	1	−57110.30	−44802.70	−60445.00	−37318.64	−127.61	621.10	−61344.72	−35250.19	−182.32	754.67
2	2	49122.68	16074.90	50015.92	17418.16	−26.98	307.58	51154.26	13937.44	51.80	93.63
3	0	−1000.82		−7680.19		−36.23		−7513.04		−31.19	
3	1	−36848.95	−21555.52	−41019.48	−27701.87	−47.24	346.25	−41495.65	−28306.26	−42.58	346.47
3	2	22617.50	35931.00	18834.47	42190.80	−37.69	72.07	20204.02	42140.24	−9.81	47.60
3	3	3736.22	−26800.52	−6546.26	−29281.84	103.65	−42.73	−8771.48	−29143.22	39.72	−40.27
4	0	−10356.79[b]		−20018.76		31.43		−20536.62		31.26	
4	1	4519.66	24942.79	6781.63	13510.19	−20.20	−6.40	7104.36	12713.96	−20.10	−6.18
4	2	−3014.04	34820.36	305.84	39420.71	5.62	−80.91	−74.44	39873.79	5.07	−79.75
4	3	−13628.22	−2931.91	−14740.31	−1278.85	29.38	2.18	−14360.38	−1676.73	26.46	4.52
4	4	−25120.85	4199.69	−15348.10	4414.59	11.01	−14.87	−14518.84	5968.78	11.74	−10.66
5	0	−18542.76		−14114.73		27.05		−14642.61		27.91	
5	1	−8066.04	16965.26	−4190.32	12109.71	7.63	−26.83	−4047.02	12837.84	7.40	−27.97
5	2	7308.83	−6347.89	13352.87	−9883.64	−25.47	19.19	13354.40	−10225.97	−25.67	20.24
5	3	−6552.56	12914.23	956.79	5483.76	−4.33	−8.64	883.19	5701.09	−3.34	−8.86
5	4	−6048.68	21930.65	−30.12	14208.50	−1.30	−27.62	363.66	13797.20	−1.84	−26.73
5	5	6332.01	13742.86	4367.76	11952.81	−8.07	−19.86	4458.32	10850.01	−7.51	−18.64
6	0	−9221.20		−7209.01		13.69		−7331.44		13.96	
6	1	−6823.99	−2616.35	−3372.35	−668.25	6.42	1.02	−3378.02	−625.41	6.43	0.98
6	2	1737.73	−1415.19	1967.91	−2688.49	−3.86	5.51	2015.02	−2727.58	−3.90	5.53
6	3	3226.16	−5219.81	2291.66	−5225.08	−4.59	9.93	2363.27	−5325.66	−4.69	10.10
6	4	2741.91	11699.95	−1328.73	6144.10	2.87	−11.66	−1456.95	5886.43	3.08	−11.28
6	5	6156.41	2993.05	3769.92	3492.18	−7.06	−6.74	3447.98	3242.49	−6.44	−6.28
6	6	−3154.92	1317.17	−718.19	124.61	1.66	−0.73	−928.19	157.77	1.84	−0.78
7	0	5033.54		2803.12		−5.42		2870.64		−5.55	
7	1	−2044.10	457.63	−2231.18	358.55	4.33	−0.64	−2299.86	363.47	4.46	−0.66
7	2	850.34	347.99	512.73	1473.82	−0.98	−2.88	523.63	1525.56	−1.00	−2.99
7	3	2000.23	−864.30	1945.55	−899.92	−3.69	1.69	1946.64	−893.28	−3.71	1.68
7	4	3371.53	−4262.56	2445.69	−2467.83	−4.64	4.77	2431.19	−2480.64	−4.62	4.79
7	5	−2700.23	2239.03	−525.51	994.72	1.00	−1.98	−600.51	1027.97	1.13	−2.02
7	6	3184.39	3610.15	3022.24	1463.84	−5.83	−2.78	2987.32	1438.44	−5.77	2.72
7	7	−125.30	−1178.63	460.96	−1412.32	−0.95	2.75	380.72	−1430.47	−0.76	2.81

[a]Given in nT and nT yr^{-1}.
[b]Coefficients here and below are recorded incorrectly in the source thesis.

damping levels, $R_{IMT} = 0.83–0.84R_J$ and conductivity dropping off over 0.05 R_J. Thus flatter spectra than those shown here can be attained, but our choices of λ, $R_{IMT} = 0.85R_J$ and $R_\alpha = 0.90R_J$ approach the values suggested by this analysis.

Figure 8 compares the misfit in B_r, B_ϕ, and B_θ as a function of radius, for the intermediate complexity **JCF** and **JSV** models. The mean residual, $\bar{x}$, standard deviation, σ, and RMS misfit are listed in Table 4. In each case, the greatest residuals are consistently found at low perijove—thus the residual increases with the magnitude of the field. This is sufficient to explain the residuals in B_r and B_ϕ, but there is a more prominent increase in fractional misfit with r for B_θ. This could relate to inadequate modeling of the magnetodisk field, in particular a failure to account for the θ_{CS} to θ_M hinging between the cold and warm torus regions. Consulting Table 4,

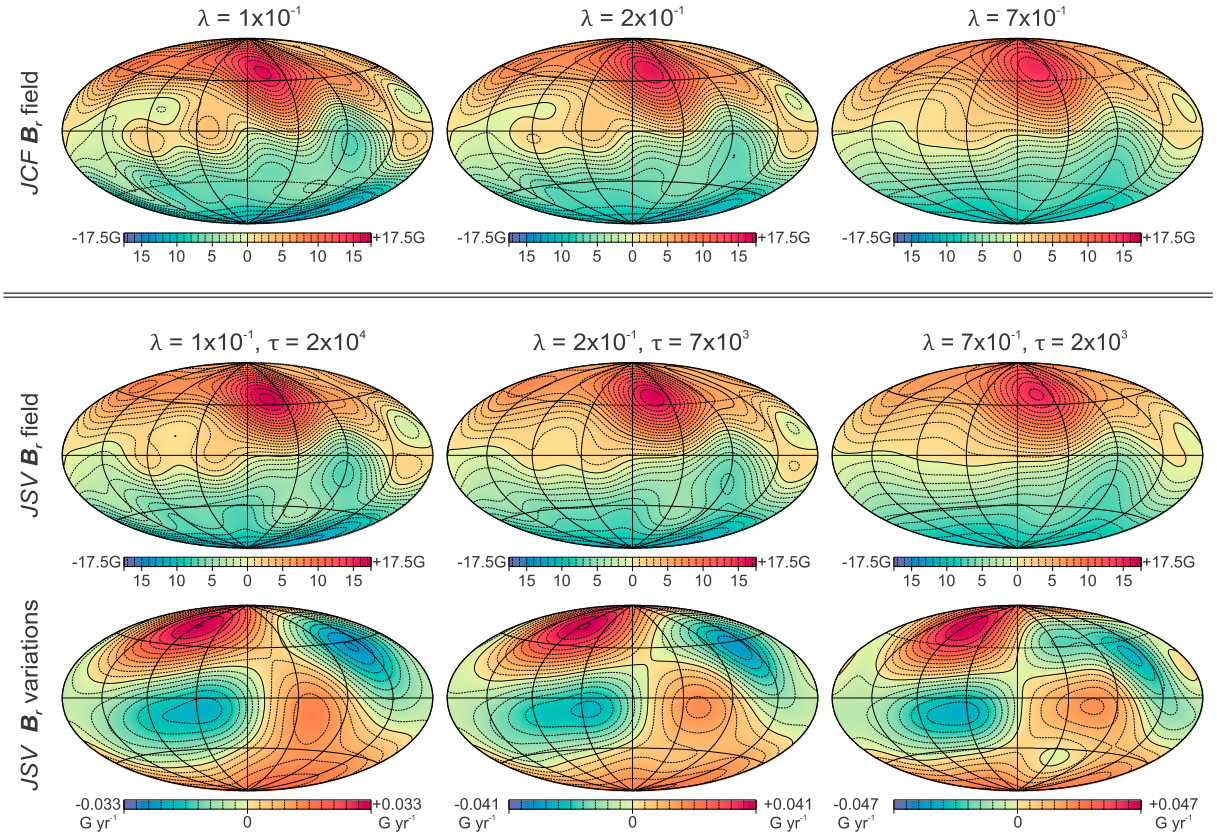

Figure 7. B_r and total modeled change in B_r for preferred **JCF** and **JSV** solutions.

misfit is not uniformly improved through employing the **JSV** approach. The B_r and B_ϕ residual has significantly lower RMS, $\bar{x}$, and σ for **JSV**, while in B_θ a minor increase in $\bar{x}$ and RMS is seen accompanying a comparable level of σ.

Further quantitative insight is provided by analysis of the coefficient resolution matrix

$$\mathbf{R} = \left(\mathbf{A}^{\mathsf{T}}\mathbf{C}_{\mathbf{e}}^{-1}\mathbf{A} + \lambda\mathbf{\Lambda}\right)^{-1}\mathbf{A}^{\mathsf{T}}\mathbf{C}_{\mathbf{e}}^{-1}\mathbf{A} \tag{10}$$

This provides a measure of how well the regularized model matches the true model in the absence of errors; it quantifies how effectively the data can resolve the model parameters. The trace of **R** provides an indication of the number of degrees of freedom in the model. Figure 6d compares the resolution for each field coefficient for the two intermediate smoothed models. The dipole field is well resolved for both types of model, with the same being true of the **JSV** variation. Up to $l = 3$ the field coefficients remain well resolved and marginally better for **JCF**, above which the parameter resolution decreases, with comparable **JCF** and **JSV R**, and by $l = 6$ no field is resolved by the data, with no resolution of SV above degree 2. At each l, higher m coefficients are better resolved, reflecting the better data coverage in longitude than in latitude. With 63 Gauss coefficients (l_{max}=7), a trace of 63 would indicate the model constrained by the data perfectly. The traces for the intermediate **JCF** and **JSV** fields are 29.22 (46%) and 27.90 (44%), respectively; this decrease signifies distribution of fit to temporal coefficients, which have a trace of 8.84 (14%). We note that the smoother **JSV** model has marginally higher SV **R**; however, the field resolution is significantly lower at 23.22 (37%).

Finally, we consider the correlation between the **JSV** field and corresponding temporal coefficients. Figure 6c shows how the correlation coefficient, r, varies for **JSV** models with smooth, intermediate, and structured λ damping, through a range of τ levels. In each case, τ of the favored **JSV** solutions are shown in black and lie close to zero, showing that for the preferred models, the estimates of field and SV are almost uncorrelated, providing evidence that our optimal models do not have leakage between the field and SV estimates.

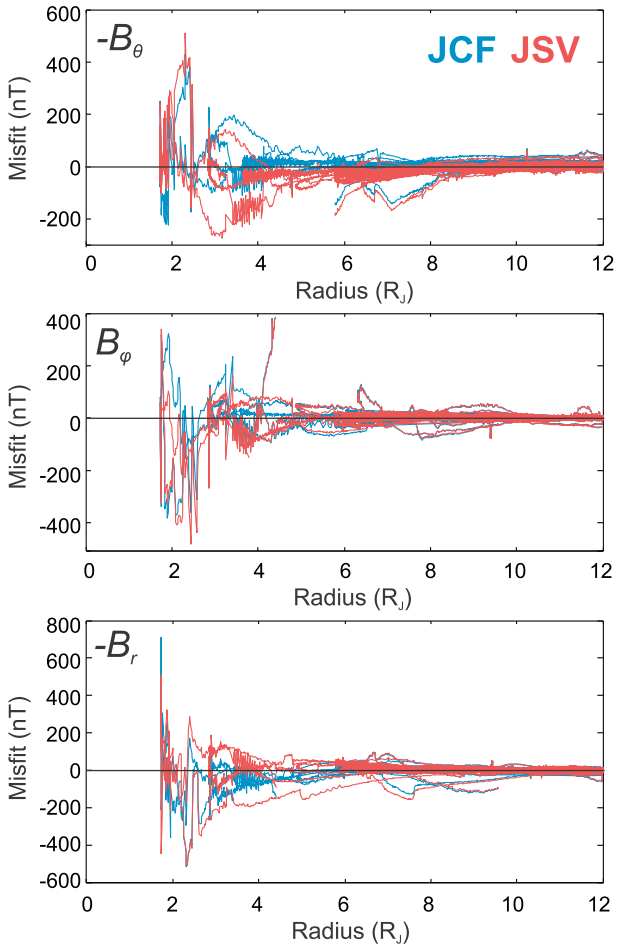

Figure 8. Model to data misfit for **JCF** and **JSV** models with intermediate field damping.

For each λ, if τ is increased by even a small amount, the correlation coefficient increases significantly, while a decrease also causes divergence of r from zero. This provides additional justification for the chosen temporal damping levels.

6.2. The Favored Solution and SV

We favor the **JSV** solutions over the **JCF** solutions and suggest that true variation can be discerned from the data. Our primary justification for this lies with the results of Figure 6b, where reduced model-to-data residual and increased field smoothness are seen when linear changes to the field coefficients are permitted. However, we acknowledge that model improvement might simply relate to the increased parameter space of the **JSV** approach. Quantifying the comparative improvement proves more insightful: the improvement in sum of squared misfit for each λ pair lies between 7 and 8%, while the relative reduction in field norm is ~2.5% for $\lambda = 7 \times 10^{-1}$, ~5% for $\lambda = 2 \times 10^{-1}$, and ~10% for $\lambda = 1 \times 10^{-1}$.

Further to this we favor the **JSV** solution with intermediate damping over the more smooth and more complex models examined. The intermediate damping resolves both the field and SV well while striking a good balance between the misfit to the data and norm. Neither temporal variation beyond the quadrupole nor field structure above $l = 5$ are well constrained, signified by both the plot of coefficient resolution and by the dropoff in power. However, inclusion of these components of the field is necessary to avoid aliasing into lower harmonic degrees.

Figure 9 plots the B_f and $\mathbf{B_h}$ of our preferred field model at Jupiter's surface. The total $\mathbf{B_h}$ at 1 R_J is greatest at lower latitudes but does not exceed 9.0 G (0.9 mT), just over half the magnitude of the maximum B_r; $\mathbf{B_h}$ is dominated by <4.5 G field. The large asymmetry in B_r surface field is even more pronounced when B_f is considered: maximum field in the north approaches 17 G, while in the south it is <12 G. Inspecting the mapped

Table 4. JCF and Average **JSV** Model Properties, for Preferred Solutions With Intermediate Field Damping ($\lambda = 2 \times 10^{-1}$)

	JCF	JSV
$\|M\|$ (G)	4.1625	4.1595
θ_M (°)	10.05	10.01
ϕ_M (°)	160.95	160.74
Maximum N $\|B_r\|$ (G)	15.89	16.70
Maximum S $\|B_r\|$ (G)	11.11	11.28
Trace of **R**	29.22	27.90
B_θ RMS	11.14	11.27
B_θ $\bar{x}$	3.11	3.60
B_θ σ	10.69	10.68
B_ϕ RMS	9.65	9.01
B_ϕ $\bar{x}$	1.66	1.56
B_ϕ σ	9.51	8.87
B_r RMS	10.75	9.72
B_r $\bar{x}$	1.76	−0.30
B_r σ	10.61	9.72

SV in B_r, B_f, and $\mathbf{B_h}$, the highest magnitude changes do not correlate with the field structure but are always found in the northern hemisphere; **JCF** and **JSV** model solutions with the same λ damping are most similar within 20° of the south pole. This asymmetry may be influenced by the availability of fewer high-latitude data from Jupiter's southern hemisphere.

Our favored model shows only a small 0.011% yr^{-1} increase in g_1^0 and larger respective decreases in g_1^1 and h_1^1 of −0.149% yr^{-1} and −0.537% yr^{-1}. This strong axial dipole stability translates to a small increase in dipole magnetic moment, $|M|$, of ∼0.013% yr^{-1} over the period of investigation and only a minor change in dipole latitude, θ_M, of 0.006° yr^{-1}. In contrast, the variation in dipole longitude, ϕ_M, is significantly larger at ∼0.122° yr^{-1}; this may reflect uncertainty in the drift of the reference system, which will be explored further.

We do not trust estimates of formal errors on the modeled field or SV (such estimates assume that the model smoothness is a hard upper bound on the true smoothness of the field, which is clearly not valid); however, the regularization acts to remove any unneeded complexity from the solutions and seeks only the minimal structure needed to fit the data, lending credence to our theory that some true magnetic secular variation is being modeled.

6.3. Comparison With Previous Models and the Geomagnetic Field

Figure 10 shows the how the dipole properties of our solution are modeled to change through time (quantified in Table 5), compared with the dipole properties from a selection of previous studies. We note that this is presented for illustrative purposes and is not a robust representation; e.g., the models constrained from data collected by multiple spacecraft or with HST images are not weighted equally between eras, but this has not been indicated.

The first notable feature seen in all plots is the range of estimates for dipole configuration, even for models constructed from data from the same epoch. The primary difference between our model and its predecessors is a generally lower estimate of dipole moment $|M|$, likely related to increased l_{max} which avoids aliasing of more complex structure into the dipole. In contrast, our implied θ_M lies in the middle of previous estimates, from the multiple models made from Pioneer data, to midway between the Ulysses models and Galileo data solutions. The small increase in dipole tilt with time found in our preferred solution may be reflected by previous results.

Examining the dipole longitude implied by different models is perhaps more interesting. We state results in east longitude for a consistent right-handed coordinate system, related to the commonly used west longitude by 180°−λ. Our solution constrains a dipole orientation of ∼159° for the Pioneer era changing to ∼162.5°

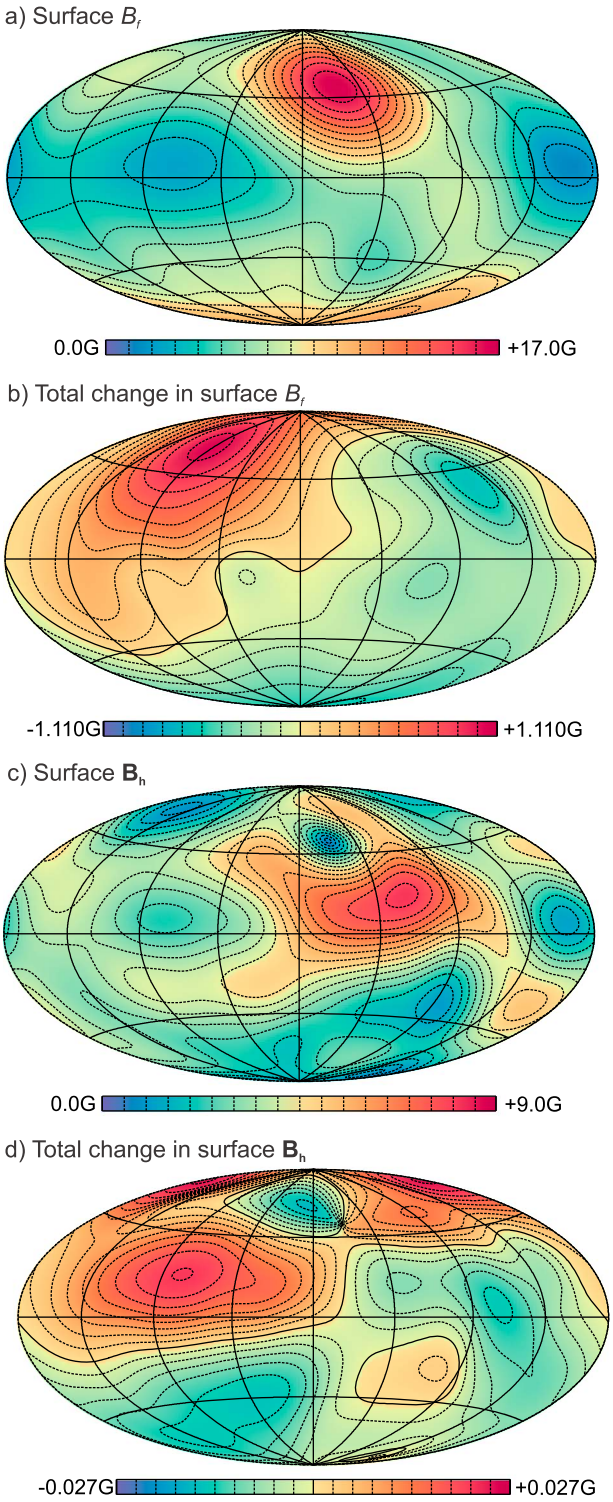

Figure 9. Total field intensity, B_r, and horizontal field, $\mathbf{B}_h$ at 1 atm, with accompanying modeled changes for the preferred **JSV** solution.

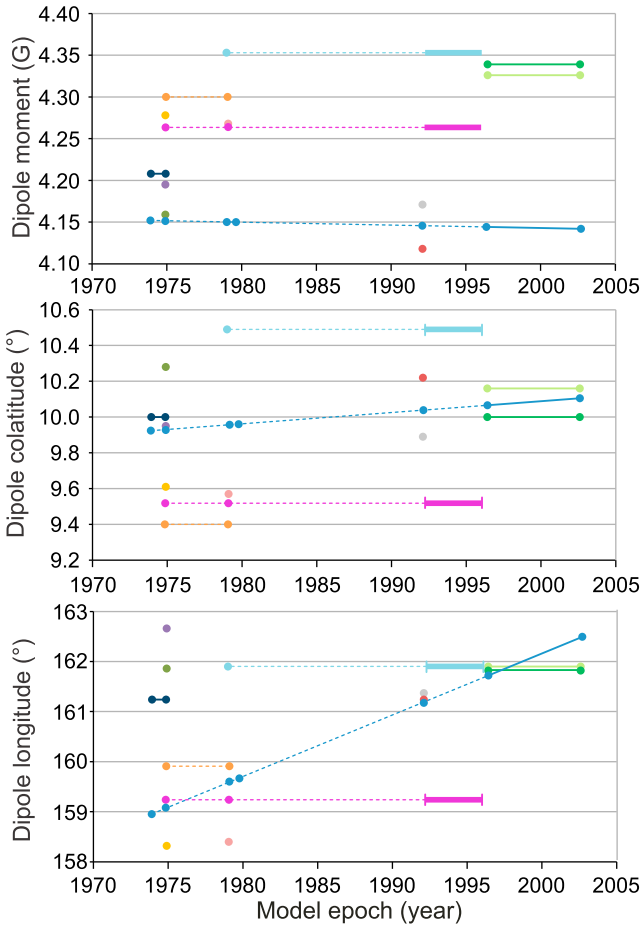

	Model/reference	Notes
●	Intermediate JSV model	This paper
●	*Davis Jr and Smith,* 1976	**P10+P11**, B_I:*l*=3, B_E:*l*=2
●	*Smith et al.,* 1975	**P11**, B_I:*l*=3, B_E:*l*=2
●	**O4** - *Acuña and Ness,* 1975	**P11**, B_I:*l*=3, B_E:*unmodelled*
●	*Connerney et al. 1982*	**V1**, B_I:*l*=3, B_E:CON1981
●	**O6** - *Connerney* 1992	**P11+V1**, B_I:*l*=6, (PS.18/48ev) B_E:CON1981
●	*Dougherty et al.* 1996	**ULY**, B_I:*l*=3, B_E:CON1981
●	*Connerney et al.*1996	**ULY**, B_I:*l*=3, (PS.12/15ev) B_E:CON1981
●	**VIP4** - *Connerney et al.* 1998	**P11+V1+Io footprint** B_I:*l*=4, (PS.20/24ev) B_E:CON1981
●	**VIT4** - *Connerney et al.* 1998	**V1+Io footprint** (like VIT4 but more weight toward footprints)
●	*Randall,* 1998	**P11+Amalthea position**
●	*Yu et al.* 2010	**GAL** B_I:*l*=3, B_E:CON1981
●	*Yu et al.* 2010	**GAL** B_I:*l*=3 (g13,h13 replaced with **O6** values), B_E:CON1981

Figure 10. Comparison of dipole properties inferred by our model and a selection of models from the literature. Circles signify timing of satellite data input; dotted lines signify data from more than one mission used. Galileo epoch signified by solid lines, circa 1996–2002. Thick solid lines for VIP4 and VIT4 show timing of Io footprint images used in model construction. "PS" stands for "partial solution."

Table 5. Implied Dipole Properties at the Start and End of Data Collection for the $\lambda = 2 \times 10^{-1}$ **JSV** Solution, With and Without the $\psi = -3.8°$ Implemented[a]

	Start $\psi = 0.0°$	Start $\psi = -3.8°$	End $\psi = 0.0°$	End $\psi = -3.8°$	Change (year^{-1}) $\psi = 0.0°$	Change (year^{-1}) $\psi = -3.8°$
g_1^0 (nT)	408987.22	408939.78	410253.52	410233.95	0.011%	0.011%
g_1^1 (nT)	−66783.92	−66765.03	−69730.22	−68082.17	0.149%	0.068%
h_1^1 (nT)	25698.55	25682.01	21993.29	26503.68	−0.537%	0.109%
$\|M\|$ (nT)	415200.02	415149.23	416718.09	416688.76	0.013%	0.013%
θ_M (°)	9.924	9.922	10.105	10.098	0.006	0.006
ϕ_M (°)	158.953	158.960	162.494	158.730	0.122	−0.008

[a]The last column, "Change" denotes the SV as a % yr^{-1} of the field attribute at time zero (∼1988.38) or a ° yr^{-1} of θ_M or ϕ_M at time zero.

by the end of Galileo. This translates to a ∼3.5° westward change over the period of investigation. If the two earliest Pioneer solutions are discounted, along with the *P*11 + Amalthea solution of *Randall* [1998], there is good agreement of a linear displacement in ϕ_M with time both among prior models and compared with our solution; this is further bolstered by the fact that **VIP4** is weighted more heavily toward the satellite data of the early era than **VIT4** [*Connerney et al.*, 1998].

Comparison of our solution with models for the geomagnetic field is difficult. Considering the 2010 Definitive Geomagnetic Reference Field (DGRF), the lowes power spectrum of the geomagnetic field flattens at the core-mantle boundary with a low quadrupole component and higher octopole, with intermediate power at $l = 4$. This is the same general configuration as that seen for our preferred model plotted at a dynamo source depth of 0.85 R_J (Figure 11) (better than 0.8 or 0.9); however, if the spectra are scaled to unit dipole power, as in Figure 11, it becomes clear that the Jovian dipole is a more dominant component of the total field than that of the Earth.

The dipole moment rate of change of 0.013% yr^{-1} seen for our preferred model is roughly one quarter of the average rate of decrease of the geomagnetic $|M|$ between 2005 and 2010 of 0.056% yr^{-1}; in the past 110 years of DGRF models, ranges between 0.020% yr^{-1} and 0.065% yr^{-1}. The 0.006° yr^{-1} change in θ_M for Jupiter is also much smaller than that seen at Earth in recent years (∼0.053° yr^{-1} between 2005 and 2010) and the mean change between DGRF solutions since 1900 of ∼0.015° yr^{-1}. In contrast, the modeled change in dipole longitude ϕ_M of ∼0.122° yr^{-1} is 3 times greater for Jupiter than Earth, which has an average rate of change since 1900 of 0.041° yr^{-1}.

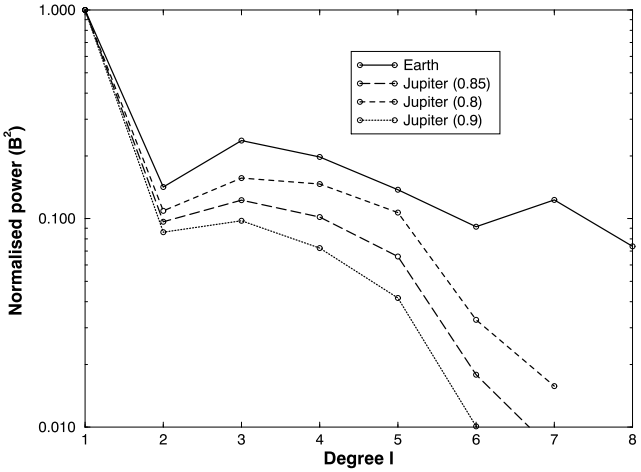

Figure 11. Magnetic field spectra for Earth (IGRF2010), plotted at core-mantle boundary (CMB), and for Jupiter (**JSV** model), plotted at depths of 0.8,0.85, and 0.9 R_J. All spectra normalized to unit power for the dipole ($l = 1$) term.

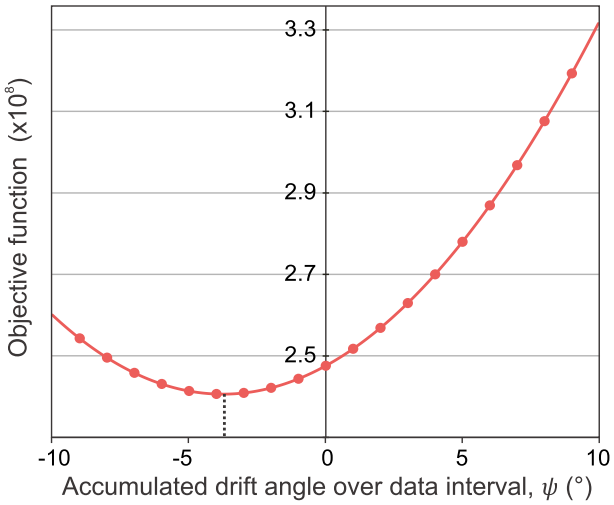

Figure 12. Preferred ψ inferred by minimized objective function when solving **JCF** with adjusted data longitude.

7. Discussion

7.1. Rotation of the Reference Frame?

While our model analysis favors the resolution of jovimagnetic secular variation from the data, the considerable change of $\phi_M = 3.5°$ leads us to investigate other explanations for our results. Similar findings in previous magnetic field studies led to the suggestion that the System III 1965.0 period of 9 h, 55 min, and 29.711 ±0.04 s, used in defining jovigraphic longitude, may be inadequate [e.g., *Yu et al.*, 2010]. Measurements of decametric radiation emitted from the Jovian magnetosphere between 1957 and 1994 have also been shown to better fit a rotation period of 9 h, 55 min, and 29.685 s [*Higgins et al.*, 1997]; this difference would induce a drift in the measurement reference frame, affecting nonzonal components of our solution SV. Here we consider whether a drift in the reference frame is suggested by our models.

We first test whether the modeling favors a linear reference frame offset rather than true SV. We calculate a range of damped **JCF** models with the longitude of each datum adjusted linearly in time by an angle proportional to a predefined drift by ψ over the period of investigation:

$$\phi_t = \phi_{1973.9} + \frac{t\psi}{T} \tag{11}$$

where ϕ_t is the adjusted longitude of a datum, t is the time of datum measurement after the first observation in ~1973.9, and T is the interval over which data collection took place, ~28.92 years. Should our objective function be significantly improved and optimized (i.e., minimal misfit and complexity) when the data are allowed to rotate through a certain ψ, this would imply that a component of the SV may be accounted for by inadequacies in constraint of the System III 1965.0 period.

Figure 12 plots how the objective function varies over a range of ψ for the intermediate damped **JCF** model. The objective function is clearly minimized when a drift of −3.8° in the reference frame is permitted by the model over the ≃28.92 year period. These values are close to the −3.5° change we have modeled in ϕ_M for the conjugate **JSV** solution but not an exact match. The presence of this discrepancy hints that the ψ drift is not solely controlled by dipole orientation, signaling dependence on additional field complexities; however, the results are strikingly close, suggesting that the modeled SV, at least in part, could reflect a change to the reference frame over the period of observation. If a linear change is assumed, the $\psi = -3.8°$ drift implies a longer rotation period, increasing System III from 9 h, 55 min, and 29.711 s to 9 h, 55 min, and 29.7258 s. This is well within the error bound of ±0.04 s put on the original System III 1965.0 value but is also contrary to the suggestion of *Higgins et al.* [1997], who preferred a decrease in the rotation rate.

To further consider possible drift of the reference frame, we look at whether longitudinally dependant field components of differing complexity have been offset by similar amounts, i.e., the nonzonal coefficients that are not symmetric about the rotation axis. First, the inferred longitudes of all g_l^m and h_l^m coefficients are

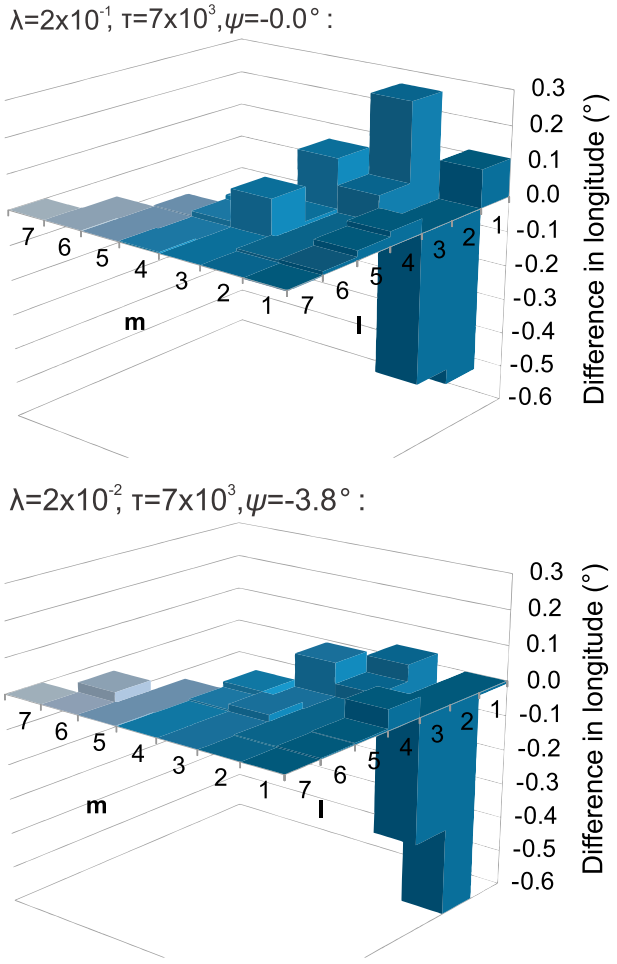

Figure 13. Inferred ψ_{lm} change of different longitudinally dependent gauss coefficient pairs over 1 year for the intermediate damped **JSV** solution with (a) $\psi = 0.0°$ and (b) $\psi = -3.8°$.

calculated at the beginning and end of the time period, from our preferred **JSV** solution. The longitudinal configuration of each conjugate pair of the same *l* and *m* can be determined as

$$\phi_{lm1973} = \tan^{-1}\left(\frac{h_l^m{}_{1973}}{g_l^m{}_{1973}}\right); \phi_{lm2003} = \tan^{-1}\left(\frac{h_l^m{}_{2003}}{g_l^m{}_{2003}}\right) \quad (12)$$

The difference between ϕ_{lm1973} and ϕ_{lm2003} then gives the change in longitude of the nonaxial field component over the period of investigation, ψ_{lm}.

Consistent ψ_{lm} for all terms would be consistent with a rotation of the reference frame relative to the System III 1965.0 period, discounting the presence of any true magnetic SV being modeled. Conversely, if there is no consistency in ψ_{lm}, it is likely that true magnetic field changes are being modeled. Furthermore, if the same can be said for the **JSV** model with the $\psi = -3.8°$ offset implemented, some true SV would again be favored even if the reference frame problems are valid.

Figure 13 plots the results of these calculations, while the coefficients for the **JSV** $\psi = -3.8°$ model are also listed in Table 3. For each model variant considered, there is clearly no correlation in ψ_{lm}. Owing to poor resolution, we expect this at high *l*, but seeing this at lower *l* suggests there has not been a uniform longitudinal drift. When the preferred $\psi = -3.8°$ is implemented, ψ_{11} is reduced to near zero but there is still some large variation for $l = 2-3$. The largest magnitude drift is consistently seen in ψ_{21} at $> -0.5°$ yr^{-1}; this angle is significantly larger than the change in ϕ_M and implies that our models favor a change in ψ_{21} of $> 14°$ between 1973 and 2003, reflecting the predominantly quadrupolar changes found through the previous spectral and surface field analysis. What could cause such a rapid variation is not clear.

This analysis again implies that a true change to the magnetic field is being resolved from the data. While a change in the reference frame with time cannot be ruled out, it cannot solely account for our modeled SV. Perhaps the simplest statement of this is that the largest individual SV coefficient is for g_2^0 and so cannot be related to changes in reference frame. Though only a linear reference frame offset has been considered here, we do not discount the possibility of nonlinear changes to the reference frame. At Earth, length of day variations take place on a range of time and magnitude scales. Just as on Earth, exchange of momentum between the atmosphere and the solid planet leads to variation in the length of day (rate of Earth rotation), similar phenomena (exchange of momentum between the near-surface atmosphere and a more rigidly rotating magnetic interior) seem plausible; however, such changes computed from possible atmospheric variation fall orders of magnitude below the observable threshold.

7.2. Further Investigation of the Northern Hemisphere Configuration

Grodent et al. [2008] compared HST observations of satellite flux tube footprints with the configuration of **VIP4** to construct an alternative model of the Jovian northern hemispheric field. The results suggested B_f to be significantly higher than previously found and also identified a small negative magnetic anomaly at $\phi \sim 120°$. The later footprint constrained, full spherical harmonic field **VIPAL** model by *Hess et al.* [2011] found similar large-scale structure in the northern hemisphere but no local reduction in field intensity analogous to the *Grodent et al.* [2008] anomaly; a maximum B_f of $\simeq$ 15 G was also found, higher than, e.g., **VIP4** ($\simeq$14 G) but less than the $\simeq$ 20 G of *Grodent et al.* [2008].

Our favored **JSV** model shows no signature of this anomaly, with distinctly smoother and lower magnitude B_f than that of *Grodent et al.* [2008]. We consider here whether this feature is present and could be revealed by reduced damping. To test this, **JCF** was remodeled over a range of lower λ, with an aim to synthesize a similar configuration and surface field strength to that seen by *Grodent et al.* [2008]. **JCF** modeling was chosen in preference to **JSV** to eliminate complexities in finding an appropriate level of temporal damping, though a similar or improved match is likely to be obtained through exploration of the latter. While an exact match was unattainable, a similar structure was found when the damping was reduced.

Figure (14a) maps B_f and B_r at the planetary surface for a solution damped a factor of 10 less than that of our preferred model. Such an underdamped model must be interpreted with care. Nevertheless, the general structure displays clear similarities to *Grodent et al.* [2008], with a slight reduction in field around 120° and a small localized increase in field around $\phi = 90–100°$. Alongside these similarities there are several discrepancies, including the lower latitude of the small $\phi = 90–100°$ feature and the field intensity at $\simeq$45° being greatly reduced. We also note that while the maximum B_f is raised to just over $\simeq$18 G, this is still below of that found by *Grodent et al.* [2008] and nearer that favored by *Hess et al.* [2011] and previous satellite data-based field models.

Mapping of B_r reveals an interesting feature. As expected, when the data are fit more closely, there is significantly more structure to B_r. Of particular interest is the field projected to the dynamo source (assuming uniform flattening of Jupiter's interior—0.06487). The results showed very low magnitude B_r but no negative field; however, doing the same for the slightly more structured **JSV** model ($\lambda = 1 \times 10^{-1}$, $\tau = 2 \times 10^4$) previously presented shows reversed flux at R_{IMT}. This is shown in Figure (14b). Similar reversed flux is not seen for other models such as **O6**, **VIP4**, and **VIPAL**, in part due to the lower l_{max} and thus lower spatial resolution of these solutions.

A polar reversed flux patch has important implications for the dynamics of Jupiter's interior. At Earth, reversed flux patches are generally favored to reflect convective upwelling in the core and may be closely linked to reversals [*Wicht and Olson*, 2004]. High-latitude reversed flux, as suggested here, has additional implications for the planetary interior and dynamics. Models of the geomagnetic field projected to the CMB display a similar region of reversed flux focused near the geographic north pole. The location of this patch is thought to relate to cyclonic structured flow and diffusive processes which reduce magnetic induction efficiency [*Finlay and Amit*, 2011]. In addition, dynamo modeling by *Stanley et al.* [2007] suggests that the configuration of field and latitudinal distribution of reversed flux may be used to constrain planetary inner-core dimensions through the control of tangential cylinder extent.

The strong similarity between our more weakly damped solution and *Grodent et al.* [2008] suggests that additional information may be present in the data and that our preferred JSV solution is smoother than need be in certain areas. The severely underdamped solution is clearly too complex: a plot of the power spectrum shows

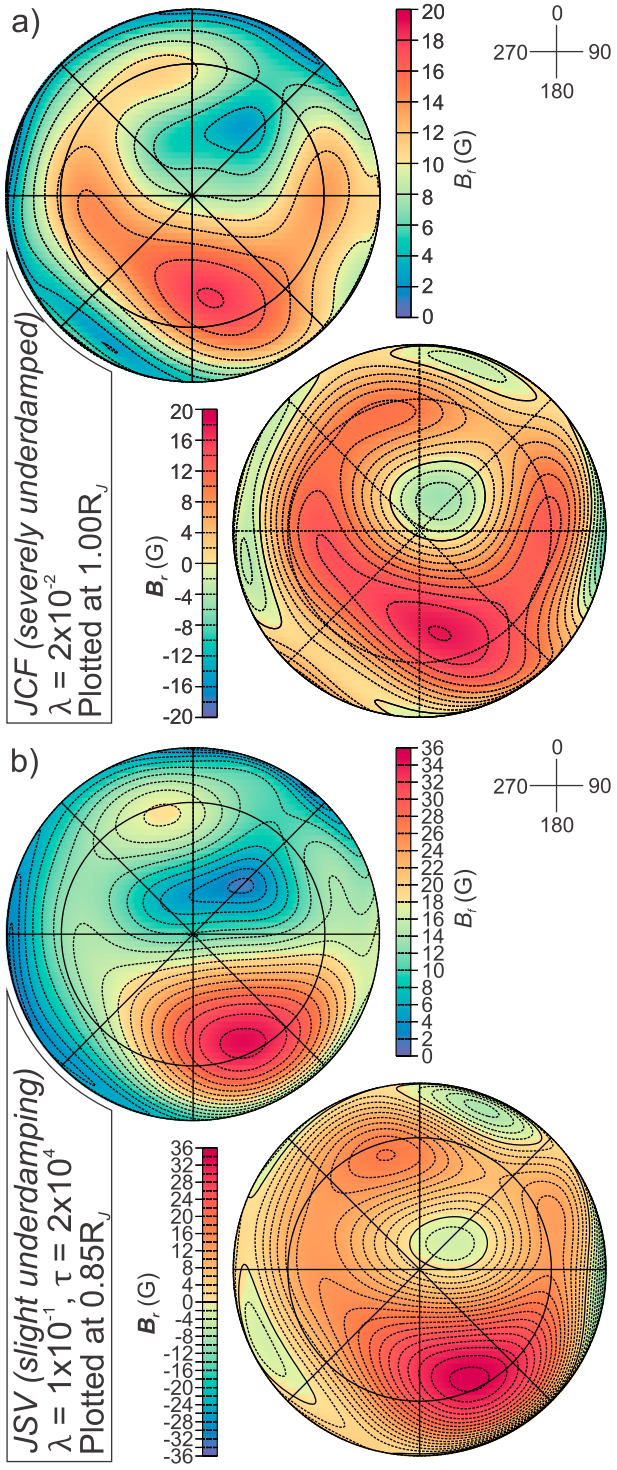

Figure 14. Comparison of northern hemisphere B_r and B_r for (a) a severely underdamped **JCF** solution at 1 R_J and (b) a very marginally underdamped **JSV** solution at 0.85R_J.

the $l = 5$ and $l = 6$ contribution to reach similar magnitude to the quadrupole. However, the slightly underdamped ($\lambda = 1 \times 10^{-1}$, $\tau = 2 \times 10^{4}$) solution is plausible. Thus, our model supports the higher detail in the northern hemisphere modeled by *Grodent et al.* [2008] and consequently the presence of a patch of reversed flux at the top of the dynamo region in Jupiter's northern hemisphere.

7.3. Modeling Interior Flow

For Earth, observed changes in the geomagnetic field are used to model core surface flows via the magnetic induction equation, which relates temporal variation of the magnetic field to convective and diffusive motion in the dynamo source [*Holme*, 2015]. The radial component is written

$$\frac{dB_r}{dt} + \nabla_H \cdot (\mathbf{v}_H B_r) = \frac{\eta}{r}\nabla^2(rB_r) \tag{13}$$

where η is the magnetic diffusivity ($1/(\mu_0\alpha)$), t is time, and $\mathbf{v}_H$ is the horizontal component of the fluid flow at the dynamo surface. In this section we use our modeled Jovian SV to infer fluid motion in Jupiter's interior. While such a extension to the work is speculative, the results provide us with a simple check that the modeled SV is reasonable. Furthermore, this is the first time that mapping interior flow from direct observational evidence has been attempted for a planet other than Earth.

Even more than for our construction of jovimagnetic field models, the inversion for flow dynamics is highly nonunique. To aid solution of Earth's core flows, it is a common practice to neglect the effect of magnetic diffusion and assume that the radial magnetic flux through the CMB is constant with time: the *frozen flux approximation* [*Roberts and Scott*, 1965]. As a consequence, the secular variation of B_r is directly related to the motion of field lines by flow, with equation (13) becoming

$$\frac{dB_r}{dt} = -\nabla_H \cdot (\mathbf{v}_H B_r) \tag{14}$$

Even after neglecting diffusion, using changes in B_r to map a flow vector at Earth's CMB remains a nonunique problem; simplistically, one equation is used to obtain two unknown components of flow. To counter this, further assumptions are commonly made to constrain the motion. Two have been used particularly often. The *tangentially geostrophic* assumption, following *Le Mouel* [1984], suggests that the fluid only experiences a small horizontal Lorentz or buoyancy force at the CMB, with its motion instead governed by the pressure gradient and Coriolis force. The second assumption of *Whaler* [1980] proposes that the flow is mainly *toroidal*, moving parallel to the CMB surface about the rotation axis. Such an assumption would be valid if the boundary of the dynamo source is stably stratified with little convective upwelling. Each of these assumptions can be employed by the inversion and, with regularization, CMB flow maps with reasonable velocities and spatial scales can be constructed for Earth. For more details, see *Holme* [2015].

We follow an identical theoretical approach to modeling Jovian internal flow. In doing so, some of the assumptions remain valid, while others are undermined by Jupiter's gaseous nature. Assuming the frozen flux theorem is supported by the minimal change between our favored **JSV** model at the start and end of the time period. Furthermore, unlike the discrete CMB at Earth, the transition at Jupiter is continuous. This has a number of implications, but two of particular significance are that vertical flow could plausibly occur and that the horizontal flow at R_{IMT} will be coupled to shallower material; the modeling does not permit or account for these dynamics in any way.

With these considerations in mind, the flow was modeled at R_{IMT} using a damped least squares fit routine. The inversion employed the temporal SV coefficients associated with our preferred **JSV** solution, with and without the $\psi = -3.8°$ adjustment in jovigraphic longitude. Both the toroidal and tangentially geostrophic assumptions were applied. Regularization was applied using the strong smoothing norm of *Bloxham* [1988], which places a constraint on the second derivative of flow velocity over R_{IMT} and strongly restricts the flow to large spatial scale. The flow was expanded in vector spherical harmonics to $l_{max} = 7$ (the same as our SV) and modeled for a range of damping levels. Trade-off curves (Figure 15) were plotted between the spatial smoothness of the flow (norm) and the residual between the **JSV** temporal coefficients and modeling the dynamics. These curves were used to establish an appropriate range of damping, but additional consideration of power spectra, velocity ranges, and flow complexity aided the final choice.

Comparison with models of Earth's flow displays common features. While other levels of damping from the trade-off curve were considered, flow strength is a sensitive function of damping; altering the level of damping by less than an order of magnitude from these favored solutions resulted in the velocities becoming either

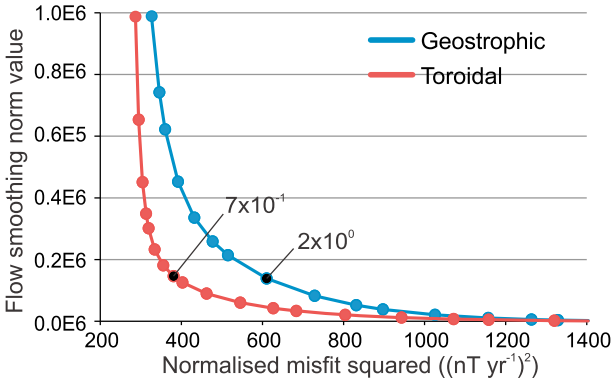

Figure 15. Trade-off curve for constraint of toroidal and geostrophic motion at dynamo surface, for preferred **JSV** model with $\lambda = 2 \times 10^{-1}$, $\tau = 7 \times 10^{3}$, and $\psi = 0.0°$. Black points indicate favored damping levels.

implausibly fast or slow. Furthermore, for these damping levels, the toroidal and tangentially geostrophic solutions are similar; at Earth, this is generally found to be the case, with very similar flow configurations [*Holme*, 2015] found independent of the modeling assumption employed. We note that there is a clear difference in both the position and shape of the trade-off curves: the toroidal assumption produces a better defined knee than tangential geostrophy, suggesting the former inversion to be better constrained. The toroidal flow is able to better fit the modeled SV; again, this is also seen for the Earth.

As this analysis is highly speculative, we do not present an exhaustive exploration of the parameter space but focus only on the preferred solutions. Figure 16 shows our preferred toroidal and tangentially geostrophic assumed flow models. There is very little difference in the flow models generated from the $\psi = -3.8°$ **JSV** model, and consequently, we plot only the favored $\psi = 0.0°$ flow. The resulting toroidal and tangentially geostrophic assumed flow solutions are similar, with comparable features appearing in both. In addition, we see a degree of symmetry about the equator, with several vortices being mirrored in both the northern and southern hemispheres; a particularly clear example of this is seen at low latitudes around $\phi = 180–210°$; again, this is consistent with Earth's core.

At Earth, symmetric gyres are often found in CMB flow models and commonly interpreted as direct observational evidence of *Busse columns* tangential cylinders dynamics in the core. Neither the method of inversion nor the smoothing norm or either the dynamic assumptions employed constrain the system in such a way to impose this structure. Thus, it seems possible that we are truly resolving columnar flow at Jupiter. These gyres and their implied surface flow are important, not only for being the first time such dynamics have been resolved for a planet other than Earth but also because their presence further helps to validate the structure of our modeled jovimagnetic secular variation.

Further validation comes by comparing the modeled flow velocities with magnitude we might expect at R_{IMT}. Theoretical studies for flow in Jupiter's metallic hydrogen interior generally suggest motion to be slower than our modeled levels. For instance, Magnetic-Archimedean-Coriolis balance estimates by *Starchenko and Jones* [2002] suggest radial convection of ~30 km yr^{-1}, with horizontal velocities additionally predicted to

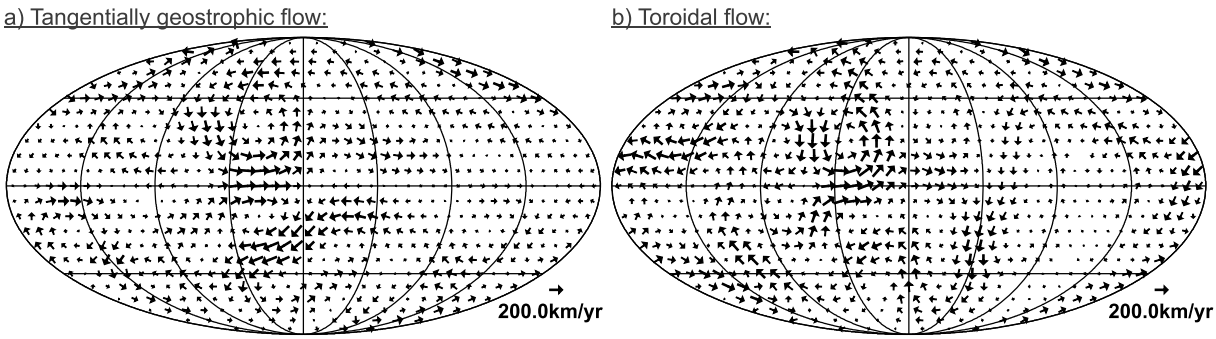

Figure 16. Optimal flow maps for preferred **JSV** solution. Plotted at dynamo source, $0.85R_J$.

approximate this magnitude. Our flow is roughly an order of magnitude larger than that theorized, though regions of our solutions do display velocities on that scale. From a different viewpoint, we follow a simple scaling argument. At Earth, flow inversions find dynamics on the order of tens of kilometers per year at the surface of the CMB [*Holme*, 2015]. At Jupiter, we are modeling similar levels of SV, while R_{IMT} is approximately 17 times larger than the radius of Earth's outer core. Based on these observations, we might expect Jovian interior velocities on the order of low-to-middle hundreds of kilometers per year, matching our models.

While our modeled flows display realistic properties, and match our expectations, we note that there are discrepancies if the flow dynamics are used to forward model resulting SV. In particular, the SV coefficient power for $l > 2$ does not drop off with increasing l but shows a gradual increase for both the toroidal and tangentially geostrophic assumptions. Further analysis with more suitable dynamical constraints, and with improved SV estimates from the Juno mission, may lend itself to a better understanding of Jupiter's deep interior structure from direct observation.

8. Conclusions

Using spacecraft data from Pioneer 10 (1973) to Galileo (2003), we have derived two types of model for Jupiter's internal planetary magnetic field: one constant over the period of observation and one which permits changes to the field linear with time. We solve the field to a higher l_{max} than previously, employing a regularized minimum norm approach, considering the use of all available data and by iteratively solving the magnetodisk field, orbit by orbit. In doing so, the solutions form the most thorough attempt to constrain internal field changes for a planet other than Earth.

Even having modeled the external field for each orbit, this is still likely to be the largest source of error in our solutions. A particular suggestion from this work would be to revise the **CON1981** model for use within the inner magnetosphere, taking into account the variation in θ_{CD} with radius. Though different spacecraft passes do favor slightly different magnetodisk configurations, on the whole, the inner magnetospheric environment appears highly stable, with no apparent dependence on solar activity. Any longer-term changes which do occur are more likely connected to Jovian system changes; a trend in our results from the Galileo period may reflect observations of changes in the rate of ion production from Io.

From analysis of our main field models, we favor that true jovimagnetic field variations can be resolved from the limited data. Of our two types of main field model, there is a 7–8% reduction in model to data RMS misfit and a 5% improvement in field smoothness when linear temporal changes are permitted; these changes are larger than might be expected if model improvement was related purely to increasing the parameter space.

The general structure of our preferred field model resembles that of previous solutions, while lowering the damping level shows similar structure to the B_f found using additional auroral satellite footprint observations. The modeled SV favors a stable dipole magnitude and dipole latitude over the ~30 year period of investigation, with the majority of resolved variation being in the quadrupole terms. The dipole changes are less than those historically found for Earth but are on the same order of magnitude. In contrast, the longitudinal component of the dipole is modeled to change by >3.5° over the period of observation, likely related to poor constraint of the Jupiter System III 1965.0 reference frame. This finding appears consistent with the longitude of previous models made from data collected at different epochs. Further analysis shows that even if a linear offset in the reference frame is accounted for during modeling, secular variation of the field is still favored.

We can conclude several things about Jupiter's internal structure using our favored solution. For the better resolved, lower l, components of our favored models, the Lowes power spectra approach a flattened state. If spectral flattening can indeed be linked to field generation source, this is consistent with a dynamo depth of $R_{IMT} = 0.85R_J$.

Our investigation of underdamped solutions hints at a reversed polar flux patch, with the interior dynamics being further explored through the construction of flow maps at the dynamo source. The solutions infer symmetrical equatorial gyres, indicative of flow on tangential cylinders, similar to that modeled from geomagnetic SV at Earth and similar to that predicted from theoretical modeling; the velocities also match that expected for Jupiter. The results from this analysis further increase our confidence in the validity of the modeled jovimagnetic SV.

The arrival of the NASA Juno mission at Jupiter in July 2016 will help answer many of the questions raised in this paper: the main field will be better resolved from observation closer to the planet, which in turn will permit far better constraint of the internal structure and dynamics. However, it remains to be seen whether the improved instrumentation and orbital trajectory will detect variation of the jovimagnetic field over the lifetime of the mission alone. Once more, it may be necessary to return to the Pioneer, Voyager, Ulysses, and Galileo measurements; if this is the case, the approach we present here is definitely of merit.

Acknowledgments
This work was funded by the Leverhulme Trust, through grant number F/00 025/AI, "Modeling the Jovian magnetic field and its variation from all available data." All data were obtained from the NASA PDS (Planetary Data System) available at https://pds.nasa.gov/ and are freely available. The free GMT software of *Wessel and Smith* [1991] was used in producing many of the plots in this paper.

References

Acuna, M., and N. Ness (1975), Jupiter's main magnetic field measured by Pioneer 11, *Nature*, *253*, 327–328.
Acuna, M., and N. Ness (1976), The main magnetic field of Jupiter, *J. Geophys. Res.*, *81*(16), 2917–2922.
Bagenal, F. (1994), Empirical model of the Io plasma torus: Voyager measurements, *J. Geophys. Res.*, *99*, 11,043–11,062.
Balogh, A., M. Dougherty, R. Forsyth, D. Southwood, E. Smith, B. Tsurutani, N. Murphy, and M. Burton (1992), Magnetic field observations during the Ulysses flyby of Jupiter, *Science*, *257*(5076), 1515–1518.
Bloxham, J. (1988), The dynamical regime of fluid flow at the core surface, *Geophys. Res. Lett.*, *15*(6), 585–588.
Bolton, S., S. Gulkis, M. Klein, I. De Pater, and T. Thompson (1989), Correlation studies between solar wind parameters and the decimetric radio emission from Jupiter, *J. Geophys. Res.*, *94*(A1), 121–128.
Brown, M., and A. Bouchez (1997), The response of Jupiter's magnetosphere to an outburst on Io, *Science*, *278*(5336), 268–271.
Bunce, E., and S. Cowley (2001), Local time asymmetry of the equatorial current sheet in Jupiter's magnetosphere, *Planet. Space Sci.*, *49*(3–4), 261–274.
Connerney, J. (1981), The magnetic field of Jupiter: A generalized inverse approach, *J. Geophys. Res.*, *86*(A9), 7679–7693.
Connerney, J. (1992), Doing more with Jupiter's magnetic field, in *Planetary Radio Emissions III*, edited by O. H. Rucker, S. J. Bauer, and M. L. Kaiser, pp. 13–33, Austria Acad. of Sci. Press, Vienna.
Connerney, J., and M. Acuna (1982), Jovimagnetic secular variation, *Nature*, *297*, 313–315.
Connerney, J., M. Acuna, and N. Ness (1981), Modeling the Jovian current sheet and inner magnetosphere, *J. Geophys. Res.*, *86*(A10), 8370–8384.
Connerney, J., M. Acuna, and N. Ness (1982), Voyager 1 assessment of Jupiter's planetary magnetic field, *J. Geophys. Res.*, *87*(A5), 3623–3627.
Connerney, J., M. Acuña, and N. Ness (1996), Octupole model of Jupiter's magnetic field from Ulysses observations, *J. Geophys. Res.*, *101*(A12), 27,453–27,458.
Connerney, J., M. Acuna, N. Ness, and T. Satoh (1998), New models of Jupiter's magnetic field constrained by the Io flux tube footprint, *J. Geophys. Res.*, *103*(6), 11,929–11,940.
Cowley, S., A. Deason, and E. Bunce (2008), Axi-symmetric models of auroral current systems in Jupiter's magnetosphere with predictions for the Juno mission, *Ann. Geophys.*, *26*, 4051–4074.
Dessler, A., and B. Sandel (1992), System III variations in apparent distance of Io plasma torus from Jupiter, *Geophys. Res. Lett.*, *19*(20), 2099–2102.
Dougherty, M., A. Balogh, D. Southwood, and E. Smith (1996), Ulysses assessment of the Jovian planetary field, *J. Geophys. Res.*, *101*(A11), 24,929–24,941.
Elphic, R., and C. Russell (1978), On the apparent source depth of planetary magnetic fields, *Geophys. Res. Lett.*, *5*(3), 211–214.
Engle, I. (1991), Idealized Voyager Jovian magnetosphere shape and field, *J. Geophys. Res.*, *96*(A5), 7793–7802.
Finlay, C., and H. Amit (2011), On flow magnitude and field-flow alignment at Earth's core surface, *Geophys. J. Int.*, *186*(1), 175–192.
Frank, L., and W. Paterson (2001), Survey of thermal ions in the Io plasma torus with the Galileo spacecraft, *J. Geophys. Res.*, *106*(A4), 6131–6149.
Giampieri, G., and M. Dougherty (2004), Modelling of the ring current in Saturn's magnetosphere, *Ann. Geophys.*, *22*, 653–659.
Goertz, C. (1976), The current sheet in Jupiter's magnetosphere, *J. Geophys. Res.*, *81*(19), 3368–3372.
Grodent, D., B. Bonfond, J. Gérard, A. Radioti, J. Gustin, J. Clarke, J. Nichols, and J. Connerney (2008), Auroral evidence of a localized magnetic anomaly in Jupiter's northern hemisphere, *J. Geophys. Res.*, *113*, A09201, doi:10.1029/2008JA013185.
Gubbins, D. (1975), Can the Earth's magnetic field be sustained by core oscillations?, *Geophys. Res. Lett.*, *2*(9), 409–412.
Guillot, T. (1999), A comparison of the interiors of Jupiter and Saturn, *Planet. Space Sci.*, *47*(10–11), 1183–1200.
Hess, S. L. G., B. Bonford, P. Zarka, and D. Grodent (2011), Model of the Jovian magnetic field topology constraint by the Io auroral emissions, *J. Geophys. Res.*, *116*, A05217, doi:10.1029/2010JA016262.
Higgins, C., T. Carr, F. Reyes, W. Greenman, and G. Lebo (1997), A redefinition of Jupiter's rotation period, *J. Geophys. Res.*, *102*, 22,033–22,041.
Holme, R. (2015), Large-scale flow in the core, in *Reference Module in Earth Systems and Environmental Sciences, Treatise on Geophys.*, 2nd ed., vol. 8, edited by G. Schubert, pp. 91–113, Elsevier, Amsterdam.
Holme, R., and J. Bloxham (1996), The magnetic fields of Uranus and Neptune: Methods and models, *J. Geophys. Res.*, *101*(E1), 2177–2200.
Khurana, K. (1992), A generalized hinged-magnetodisc model of Jupiter's nightside current sheet, *J. Geophys. Res.*, *97*(A5), 6269–6276.
Klein, M., S. Bolton, S. Gulkis, M. Janssen, S. Levin, J. Roller, and R. McLeod (2001), Cassini-Jupiter microwave observing campaign: DSN and GAVRT observations of Jovian synchrotron radio emission, in *Planetary Radio Emissions V*, vol. 1, edited by H. O. Rucker, M. L. Kaiser, and Y. LeBlanc, pp. 221–228, Austrian Acad. of Sci. Press, Vienna.
Krupp, N., et al. (2004), Dynamics of the Jovian magnetosphere, in *Jupiter: The Planet, Satellites and Magnetosphere*, vol. 1, edited by F. Bagenal, T. E. Dowling, and W. B. McKinnon, pp. 617–638, Cambridge Univ. Press, Cambridge, U. K.
Le Mouel, J. (1984), Outer-core geostrophic flow and secular variation of Earth's geomagnetic field, *Nature*, *311*, 734–735.
Lowes, F. (1974), Spatial power spectrum of the main geomagnetic field, and extrapolation to the core, *Geophys. J. R. Astron. Soc.*, *36*(3), 717–730.
Nellis, W. (2000), Metallization of fluid hydrogen at 140 GPa (1.4 Mbar): Implications for Jupiter, *Planet. Space Sci.*, *48*(7–8), 671–677.
Nellis, W., M. Ross, and N. Holmes (1995), Temperature measurements of shock-compressed liquid hydrogen: Implications for the interior of Jupiter, *Science*, *269*(5228), 1249.
Nellis, W., S. Weir, and A. Mitchell (1996), Metallization and electrical conductivity of hydrogen in Jupiter, *Science*, *273*(5277), 936–938.
Nettelmann, N., B. Holst, A. Kietzmann, M. French, R. Redmer, and D. Blaschke (2008), Ab initio equation of state data for hydrogen, helium, and water and the internal structure of Jupiter, *Astrophys. J.*, *683*, 1217–1228.

Pontius, D., Jr. (1995), Implications of variable mass loading in the Io torus: The Jovian flywheel, *J. Geophys. Res.*, *100*(A10), 19,531–19,539.
Randall, B. (1998), An improved magnetic field model for Jupiter's inner magnetosphere using a microsignature of Amalthea, *J. Geophys. Res.*, *103*(A8), 17,535–17,542.
Roberts, P., and S. Scott (1965), On analysis of the secular variation, *J. Geomagn. Geoelectr.*, *16*(2), 137–151.
Russell, C., and M. Kivelson (2001), Evidence for sulfur dioxide, sulfur monoxide, and hydrogen sulfide in the Io exosphere, *J. Geophys. Res.*, *106*(E12), 33,267–33,272.
Russell, C., Z. Yu, and M. Kivelson (2001), The rotation period of Jupiter, *Geophys. Res. Lett.*, *28*(10), 1911–1912.
Sandel, B., and A. Broadfoot (1982), Discovery of an Io-correlated energy source for Ios hot plasma torus, *J. Geophys. Res.*, *87*(A4), 2231–2240.
Shure, L., R. Parker, and G. Backus (1982), Harmonic splines for geomagnetic modelling, *Phys. Earth Planet. Inter.*, *28*(3), 215–229.
Smith, E., L. Davis Jr., D. Jones, P. Coleman Jr., D. Colburn, P. Dyal, and C. Sonett (1975), Jupiter's magnetic field, magnetosphere, and interaction with the solar wind: Pioneer 11, *Science*, *188*(4187), 451–455.
Smith, E., L. Davis Jr., and D. Jones (1976), Jupiter's magnetic field and magnetosphere, in *IAU Colloquium 30: Jupiter: Studies of the Interior, Atmosphere, Magnetosphere and Satellites*, vol. 1, edited by T. Gehrcls, pp. 788–829, Univ. of Ariz. Press, Tucson, 19–21 May.
Stanley, S., M. Zuber, and J. Bloxham (2007), Using reversed magnetic flux spots to determine a planet's inner core size, *Geophys. Res. Lett.*, *34*, L19205, doi:10.1029/2007GL030892.
Starchenko, S., and C. Jones (2002), Typical velocities and magnetic field strengths in planetary interiors, *Icarus*, *157*(2), 426–435.
Sterenborg, M., and J. Bloxham (2010), Can Cassini magnetic field measurements be used to find the rotation period of Saturn's interior?, *Geophys. Res. Lett.*, *37*, L11201, doi:10.1029/2010GL043250.
Thomas, N., F. Bagenal, T. Hill, and J. Wilson (2004), The io neutral clouds and plasma torus, in *Jupiter. The Planet, Satellites and Magnetosphere*, vol. 1, edited by F. Bagenal, T. E. Dowling, and W. B. McKinnon, pp. 561–591, Cambridge Univ. Press, Cambridge, U. K.
Uno, H., C. Johnson, B. Anderson, H. Korth, and S. Solomon (2009), Modeling Mercury's internal magnetic field with smooth inversions, *Earth Planet. Sci. Lett.*, *285*(3–4), 328–339.
Weir, S., A. Mitchell, and W. Nellis (1996), Metallization of fluid molecular hydrogen at 140 GPa (1.4 Mbar), *Phys. Rev. Lett.*, *76*(11), 1860–1863.
Wessel, P., and W. Smith (1991), Free software helps map and display data, *Eos Trans. AGU*, *72*, 441–446.
Whaler, K. (1980), Does the whole of the Earth's core convect?, *Nature*, *287*, 528–530.
Wicht, J., and P. Olson (2004), A detailed study of the polarity reversal mechanism in a numerical dynamo model, *Geochem. Geophys. Geosyst.*, *5*, Q03H10, doi:10.1029/2003GC000602.
Yu, Z., H. Leinweber, and C. Russell (2010), Galileo constraints on the secular variation of the Jovian magnetic field, *J. Geophys. Res.*, *115*, E03002, doi:10.1029/2009JE003492.

Erratum

In the originally published version of this article, Table 3 had two numerical errors in column 4. In addition, four values in columns 3 and 4 of the HTML version of Table 4 were missing minus signs. The errors have since been corrected and this version may be considered the authoritative version of record.